The Astrophysical Journal, 873:20 (21pp), 2019 March 1 https://doi.org/10.3847/1538-4357/ab0209

The SOMA Radio Survey. I. Comprehensive SEDs of High-mass Protostars from Infrared to Radio and the Emergence of Ionization Feedback

V. Rosero[1,2,3], K. E. I. Tanaka[3,4,5], J. C. Tan[2,6], J. Marvil[1], M. Liu[2,3], Y. Zhang[7], J. M. De Buizer[8], and M. T. Beltrán[9]

[1] National Radio Astronomy Observatory, 1003 Lopezville Rd., Socorro, NM 87801, USA
[2] Department of Astronomy, University of Virginia, Charlottesville, VA 22904, USA
[3] Department of Astronomy, University of Florida, Gainesville, FL 32611, USA
[4] Department of Earth and Space Science, Osaka University, Toyonaka, Osaka 560-0043, Japan
[5] ALMA Project, National Astronomical Observatory of Japan, Mitaka, Tokyo 181-8588, Japan
[6] Department of Space, Earth and Environment, Chalmers University, SE-412 96 Gothenburg, Sweden
[7] Star and Planet Formation Laboratory, RIKEN Cluster for Pioneering Research, Wako, Saitama 351–0198, Japan
[8] SOFIA–USRA, NASA Ames Research Center, MS 232–12, Moffett Field, CA 94035, USA
[9] INAF, Osservatorio Astrofisico di Arcetri, Largo E. Fermi 5, I-50125 Firenze, Italy
Received 2018 September 4; revised 2019 January 24; accepted 2019 January 25; published 2019 February 28

Abstract

We study centimeter continuum emission of eight high- and intermediate-mass protostars that are part of the *SOFIA* Massive Star Formation Survey, thus building extended spectral energy distributions (SEDs) from the radio to the infrared. We discuss the morphology seen in the centimeter continuum images, which are mostly derived from archival Very Large Array data, and the relation to infrared morphology. We use the SEDs to test new models of high-mass star formation including radiative and disk-wind feedback and associated free–free and dust continuum emission. We show that interferometric data of the centimeter continuum flux densities provide additional, stringent tests of the models by constraining the ionizing luminosity of the source; they also help to break degeneracies encountered when modeling the infrared-only SEDs, especially for the protostellar mass. Our derived parameters are consistent with physical parameters estimated by other methods, such as dynamical protostellar masses. We find a few examples of additional stellar sources in the vicinity of the high-mass protostars, which may be low-mass young stellar objects. However, the stellar multiplicity of the regions, at least as traced by radio continuum emission, appears to be relatively low.

Key words: ISM: jets and outflows – stars: formation – techniques: interferometric

1. Introduction

High-mass stars ($m_* \geqslant 8\,M_\odot$) are important throughout astrophysics, but their mechanism of formation is still actively debated—see, e.g., Tan et al. (2014) for a review. For traditional star formation models based on core accretion, there is a proposed evolutionary sequence as the protostar grows in mass. For example, based on the Turbulent Core Accretion model (McKee & Tan 2003), Zhang et al. (2014) and Zhang & Tan (2018) have presented a sequence of protostellar evolution and infrared continuum radiative transfer models exclusively developed for intermediate and high-mass stars. These can be compared to observed infrared and sub-mm spectral energy distributions (SEDs) and images to constrain the properties of the protostar (e.g., Zhang et al. 2013; De Buizer et al. 2017).

High-mass protostars are generally expected to become fairly bright centimeter continuum sources (flux densities of ∼few mJy to Jy), as the stellar photosphere heats up and begins to ionize its surroundings. Centimeter continuum observations, especially with the improved capabilities of the Karl G. Jansky Very Large Array (VLA),[10] are therefore able to provide unique insights into the earliest, embedded phases of high-mass star birth. Moreover, Tanaka et al. (2016) (hereafter TTZ16) calculated the predicted ionization structures and centimeter continuum emission properties using the initial parameters resulting from the radiative transfer models. In this framework, the earliest stages of ionizing feedback involve the ionization of a magnetohydrodynamical driven disk wind and/or X-wind, which would appear as a thermal radio jet (see also Tan & McKee 2003). Later, once the outflow is fully ionized, the ionizing photons begin to interact with the infall envelope and disk, potentially driving a photoevaporative outflow. Alternative models have been discussed in the literature, including those involving ionized accretion flows at the center of the core (Keto 2007). More radically, alternative formation scenarios invoking competitive accretion (Bonnell et al. 2001; Wang et al. 2010) or even protostellar collisions (Bonnell et al. 1998; Bally & Zinnecker 2005) are expected to involve much more disordered accretion flows to the protostar (see also Dale et al. 2005) and these may become illuminated by their radio emission once the protostars start ionizing their surroundings.

High-mass star-forming regions are composed of one or more cores or dense substructures occupying $\lesssim$0.1 pc scales. When there are multiple sources present, these may be in different evolutionary stages, from prestellar to protostellar. The latter begin to show greater astrochemical complexity as the protostar warms up the inner region, appearing as hot molecular cores (HMCs). Rosero et al. (2016), using the VLA and achieving image rms noise values of ∼3–10 μJy/beam, found that HMCs are very commonly associated with centimeter wavelength sources, most of them with low radio emission levels on the order of <1 mJy. Moreover, many of these centimeter continuum sources have morphologies and parameters that resemble ionized jets, which is in general

[10] The National Radio Astronomy Observatory is a facility of the National Science Foundation, operated under cooperative agreement by Associated Universities, Inc.

agreement with results from the TTZ16 modeling. Thus, radio continuum emission is extremely relevant when constraining the ionizing luminosity of the protostar.

Physical parameters, such as the mass of the hosting core, the mass of the central protostar, and the mass accretion rate, are extremely important to characterize the evolution of forming high-mass stars, but obtaining accurate estimates of these parameters is rather challenging. Thus, the testing and calibration of new theoretical models that predict such parameters using observational data are urgently needed. Our overall goal now is to assemble multiwavelength data for a statistically significant sample of high- and intermediate-mass protostars and use these data to test theoretical models of their formation and feedback mechanisms. Our sample will probe different environments, evolutionary stages, and core masses using observations from the MIR, FIR, sub-mm/mm, and centimeter wavelengths. The *SOFIA* Massive (SOMA) Star Formation Survey (PI: Tan) aims to observe ∼50 high- and intermediate-mass protostars with *SOFIA*-FORCAST at ∼10–40 μm. Such data, together with ancillary *Herschel* data, help define the peak of the SED, thus constraining the bolometric luminosity of the protostars. Furthermore the ∼10–40 μm images trace warm dust delineating protostellar outflow cavities, which helps to determine the geometry of the protostellar source. Extinction of this cavity emission by the colder, dense core envelope also constrains properties of the protostellar core. The SOMA survey sample consists of a range of four source types that have been defined in De Buizer et al. (2017) (i.e., Type I to Type IV), from isolated MIR sources within otherwise infrared dark clouds lacking centimeter continuum emission (i.e., Type I) at an image rms level ∼0.3 mJy/beam (typical of the CORNISH survey; Purcell et al. 2008), to more evolved sources with known centimeter continuum emission of various extents (i.e., Type II and Type III for association with hypercompact (HC) or ultracompact (UC) H II regions, respectively), to clustered (within ∼60″) MIR sources that are sometimes known to be associated with radio emission (i.e., Type IV). So far, 22 sources from the SOMA survey have been observed with *SOFIA*-FORCAST and results for the first eight protostars from the sample are presented in De Buizer et al. (2017) (hereafter DLT17). These results include the derivation of SEDs and then model fitting using the theoretical Zhang & Tan (2018) (hereafter ZT18) models developed exclusively for high- and intermediate-mass protostars. In particular, the protostellar mass, accretion rate, and core envelope mass are estimated. The geometries of the cores are also constrained: e.g., the near-facing, blue-shifted side of the outflow has a cavity that typically appears brighter at shorter IR wavelengths compared to the far-facing, redshifted side. However, there are still significant degeneracies in parameters derived from infrared SEDs alone, such as the protostellar masses and bolometric luminosities that, even for the best models have relatively large allowed ranges. Our goal with this study is to use the centimeter emission data and the associated predictions of centimeter continuum free–free emission from TTZ16 to help break these degeneracies.

Previous observational studies such as the Red *MSX* Source (RMS) survey (e.g., Hoare et al. 2005; Mottram et al. 2007; Urquhart et al. 2009) have made progress toward multi-wavelength observations and studies of high-mass protostars located throughout the Galaxy. Their observations are mainly based upon the *Midcourse Space Experiment* (*MSX*) survey (Price et al. 2001) and Two Micron All Sky Survey data for the infrared, as well as centimeter continuum from the VLA at 6 cm with spatial resolutions of ∼1″–2″ and image rms noise of ∼0.22 mJy. However, our FORCAST data has ∼6× higher resolution that the *MSX* survey at ∼20 μm, and we are often resolving multiple sources of emission that appear as single sources in *MSX*, allowing for more precise photometry. Also, with the FORCAST data, we have extended the wavelength coverage of the SEDs beyond the longest filter of *MSX*, which was 21.3 μm. Furthermore, the FORCAST filters have narrower bandpasses, and are therefore more accurate at estimating the flux at a given wavelength.

Previous relevant theoretical studies have included numerical simulations of massive star formation that incorporate MHD outflow feedback (e.g., Cunningham et al. 2011; Kuiper et al. 2016; Matsushita et al. 2017; Kölligan & Kuiper 2018; Kuiper & Hosokawa 2018; Staff et al. 2018). However, in general, the outputs of these simulations have not been coupled to detailed radiative transfer calculations for both the thermal dust and radio continuum (free–free) emission from ionized gas, nor do these models span a wide range of environmental conditions. Thus, our approach in this paper is to use the observational data to test simpler semianalytic models, i.e., the ZT18 grid of models for thermal dust emission from massive protostars and the TTZ16 models for radio continuum emission from ionized gas calculated self-consistently from the ZT18 physical models.

In this paper, we present SEDs that have been extended to include centimeter continuum fluxes for the eight regions studied by DLT17, and which are under the SOMA Type II category, specifically because the MIR emission extends beyond the observed radio emission. All these sources are known to be associated with large-scale molecular outflows—except for IRAS 07299−1651, due to its limited observational data. We primarily used high-sensitivity Jansky VLA public archival data at 6, 1.3, and 0.7 cm to determine the flux densities of the regions in order to test the TTZ16 model. We used information from the literature when the regions did not have any public Jansky VLA data available. In order to investigate the morphology and the multiplicity of the radio sources associated with our eight SOMA regions, we focused on available high angular resolution data; in most cases, the data presented in this paper at the shorter wavelengths are ∼10× higher resolution than at larger wavelengths. The methodology and public archival data are presented in Section 2. A description of the TTZ16 models is in Section 3. Basic observational results are presented in Section 4, while analysis and testing of the TTZ16 models are in Section 5. The discussion and summary are presented in Sections 6 and 7, respectively.

2. Methods

The SOMA Star Formation Survey sample is defined by *SOFIA*-FORCAST observations (i.e., from ∼10 to 40 μm), with the first eight sources presented by DLT17. These eight sources define the sample for which we present and analyze the radio data in this paper. The radio observations presented here are mostly public Jansky VLA data retrieved from the VLA data archive—except for regions G45.47+0.05 (at 6 cm) and Cepheus A, where we used information available in the literature, as well as region IRAS 07299−1651, where we present our own observations.

The archival and literature data that we analyzed in this work are summarized in Table 1. Column 1 gives the region name; columns 2, 3, and 4 give the band frequency, R.A., and decl.,

Table 1
SOMA Sources: Radio Continuum Data

Region	Frequency Band (GHz)	R.A. (J2000)	Decl. (J2000)	Beam Size ($'' \times ''$, degree)	rms (μJy beam^{-1})	D[a] (kpc)	L[b] (10^4 $L_\odot$)	References[c]
AFGL 4029	4.0−8.0	03 01 31.28	+60 29 12.9	0.35 × 0.28, −43.7	7.0	2.0	1.6−34.0	...
	40.0−50.0	...	...	0.06 × 0.04, +69.7	60.0	...	...	...
AFGL 437	4.0−8.0	03 07 24.55	+58 30 52.8	0.44 × 0.33, −76.0	7.0	2.0	1.7−15.0	...
	40.0−50.0	...	...	0.06 × 0.04, +71.7	60.0	...	...	...
IRAS 07299−1651	4.0−8.0	07 32 09.74	−16 58 11.3	0.47 × 0.29, −9.84	7.0	1.68	1.0−4.2	...
	...	...	...	...	...	...	...	...
G35.20−0.74	4.0−8.0	18 58 13.02	+01 40 36.2	0.54 × 0.28, −48.5	8.0	2.2	3.8−8.4	...
	18.0−26.5	...	...	0.30 × 0.25, −12.8	18.0	...	...	...
	40.0−50.0	...	...	0.17 × 0.13, −29.1	15.0	...	...	...
G45.47+0.05	6 cm[d]	19 14 25.67	+11 09 25.4	1.75 × 1.57, −78.9	1000.0	8.4	17.0−51.0	(1)
	40.0−50.0	...	...	0.05 × 0.04, −24.2	90.0	...	...	...
IRAS 20126+4104	4.0−8.0	20 14 26.05	+41 13 32.5	0.33 × 0.29, +65.2	6.0	1.64	2.0−9.3	(2)
	18.0−26.5	...	...	0.35 × 0.24, −85.1	10.0	...	...	...
Cepheus A	3.6 cm[d]	22 56 17.98	+62 01 49.4	0.27 × 0.19, −79.1	50.0	0.7	2.4−9.9	(3)
	1.3 cm[d]	...	...	0.09 × 0.07, +32.8	50.0	...	...	...
	0.7 cm[d]	...	...	0.05 × 0.04, −57.9	250.0	...	...	...
NGC 7538 IRS9	4.0−8.0	23 14 01.77	+61 27 19.8	0.32 × 0.26, +20.7	30.0	2.65	3.7−8.2	...
	40.0−50.0	...	...	0.05 × 0.04, −5.29	43.0	...	...	...

Notes. The centimeter continuum information of sources G45.47+0.05 (at 6 cm) and Cepheus A were taken from the literature, and the references are given in column 9. Also, for the analysis of IRAS 20126+4104, we use the radio images presented in Rosero et al. (2016). Units of R.A. are hours, minutes, and seconds, and units of decl. are degrees, arcminutes, and arcseconds.
(1) Urquhart et al. (2009); (2) Rosero et al. (2016); (3) Curiel et al. (2006).
[a] References cited in De Buizer et al. (2017).
[b] Range of bolometric luminosities from the best models reported in De Buizer et al. (2017).
[c] References for the literature data.
[d] Value from the literature. Data observed using the VLA before the upgrade.

respectively; columns 5 and 6 respectively give the synthesized beam size and position angle (PA) and the rms of the resulting images. The distance to every region, as adopted by DLT17, as well as the bolometric luminosities evaluated by DLT17, are shown in columns 7 and 8, respectively.

The references for the radio fluxes that were obtained from the literature are in column 9. A list of phase calibrators used in the observations at 6, 1.3, and 0.7 cm is given in Table 2.

2.1. VLA Data

2.1.1. The 6 cm Data

The 6 cm (*C*-band) observations were made in the A configuration, providing angular resolutions ∼0.″3–0.″5. The data for sources AFGL 4029, AFGL 437, and NGC 7538 IRS9 are from project code 12B–140 from observations taken in 2012 and the data for source G35.20−0.74 are from project code 13B–210 from observations taken in 2013. The data consist of two 1 GHz wide basebands (8 bit samplers) centered at 5.3 and 6.3 GHz, where each baseband was divided into 8 spectral windows (SPWs), each with a bandwidth of 128 MHz. The data were recorded in 16 unique SPWs, each comprised of 64 channels and each channel being 2 MHz wide, resulting in a total bandwidth of 2048 MHz (before "flagging"). Source 3C48 was used as flux density and bandpass calibrator for regions AFGL 4029 and AFGL 437, and 3C286 was used as flux density and bandpass calibrator for regions G35.20−0.74 and NGC 7538 IRS9. For sources AFGL 4029, AFGL 437, and NGC 7538 IRS9, the observations were made alternating on a target source for ∼13 minutes and a phase calibrator for ∼1 minute, for a total on-source time of ∼26 minutes. For G35.20−0.74, the observations were made alternating on a target source for ∼10 minutes and a phase calibrator for ∼1 minute, for a total on-source time of ∼40 minutes.

Table 2
VLA Calibrators

Calibrator	Astrometry Precision[a]	Source Calibrated	Band
J0228+6721	A	AFGL 4029	*C, K, Q*
J0359+5057	B	AFGL 437	*C, K*
J2230+6946	A	NGC 7538 IRS9	*C, K*
J0735−1735	A	IRAS 07299−1651	*C*
J1851+0035	C	G35.20−0.74	*C, K*
J0228+6721	A	AFGL 437	*Q*
J1924+1540	A	G45.47+0.05	*Q*
J2250+5550	A	NGC 7538 IRS9	*Q*

Note.
[a] Astrometric precisions of A, B, and C correspond to positional accuracies of <2 mas, 2–10 mas, and 0.01–0.15 arcsec, respectively.

The observations for source IRAS 07299−1651 are from project code 18A–294 (PI: Rosero) taken in 2018 and the data consist of two ∼2 GHz wide basebands (3 bit samplers) centered at 5.03 and 6.98 GHz. The data were recorded in 30 unique SPWs, each comprised of 64 channels and each channel being 2 MHz wide, resulting in a total bandwidth of 3842 MHz (before "flagging"). Source 3C48 was used as flux density and bandpass calibrator, and the observations were made alternating on a target source for ∼9.5 minutes and a phase calibrator for ∼40 s, for a total on-source time of ∼37 minutes.

The data were processed using NRAO's Common Astronomy Software Applications (CASA)[11] package. Eight channels

[11] http://casa.nrao.edu

at the edges of each baseband were flagged due to substantial band roll-off (and consequent loss of sensitivity). In addition, we inspected the data for radio frequency interference or other problems, performing "flagging" when needed. The flux density scale was set via standard NRAO models, using the task `setjy` for the flux calibrators and applying the Perley & Butler (2013) flux scale. We used the `gencal` task to check for antenna position corrections and also to apply gain curve and antenna efficiency factors. Delay and bandpass solutions were formed based on observations of the flux density calibrator. These solutions were applied when solving for the final amplitude and phase calibration using the task `gaincal` over the full bandwidth. We measured the flux density of the phase calibrators using the task `fluxscale`. The amplitude, phase, delay, and bandpass solutions were applied to the target sources using the task `applycal`. The images were made using the `tclean` task and Briggs `Robust` = 0.5 weighting. For source G35.20−0.74, we performed self-calibration.

For regions AFGL 4029, AFGL 437, G35.20−0.74, and NGC 7538 IRS9, we made two images, each of a ∼1 GHz baseband composed of 8 SPWs, and also a combined image using data from both basebands with a total of 16 SPWs. For region IRAS 07299−1651, we made two images, each of a ∼2 GHz baseband composed of 15 SPWs, and also a combined image using data from both basebands with a total of 30 SPWs. All maps were primary-beam-corrected. Columns 5 and 6 of Table 1 show the synthesized beam (size and position angle) and the rms of the combined images.

2.1.2. The 1.3 cm Data

The 1.3 cm (*K*-band) observations were made in the B configuration, providing angular resolutions 0.″3. The data reduced in this work are for source G35.20−0.74 (project code 13B–033), from observations taken in 2013. The data consist of two 4 GHz wide basebands (3 bit samplers) centered at 19.9 and 23.9 GHz, where each baseband was divided into 32 SPWs, each with a bandwidth of 128 MHz. The data were recorded in 64 unique SPWs, each comprised of 128 channels and each channel being 1 MHz wide, resulting in a total bandwidth of 8192 MHz (before "flagging"). Source 3C286 was used as the flux density and bandpass calibrator for region G35.20−0.74. The observations were made alternating on a target source for ∼2.5 minutes and a phase calibrator for ∼1 minute, for a total on-source time of ∼7 minutes.

The data reduction was done in the same fashion as that for the 6 cm observations. In addition, we corrected for atmospheric opacity by using weather station information from the `plotWeather` task and creating a calibration table using `gencal`. The images were made using the `tclean` task and Briggs `Robust` = 0.5 weighting. We made two images, each of a ∼4 GHz baseband composed of 32 SPWs, and also a combined image using data from both basebands with a total of 64 SPWs. All maps were primary-beam-corrected. Table 1 columns 5 and 6 show the synthesized beam (size and position angle) and the rms of the combined images.

2.1.3. The 0.7 cm Data

The 0.7 cm (*Q*-band) observations were made in the A configuration except for G35.20−0.74, where the B configuration was used, providing angular resolutions ∼0.″04–0.″06 and ∼0.″2 for the B configuration data. The data for sources AFGL 4029 and AFGL 437 are from project code 15A–238 from observations taken in 2015, the data for source G35.20−0.74 are from project code 13B–210 from observations taken in 2013, the data for source G45.47+0.05 are from project code 14A–113 from observations taken in 2014, and the data for source NGC 7538 IRS9 are from project code 14A–092 from observations taken in 2014. The data for sources AFGL 4029, AFGL 437 and NGC 7538 IRS9 consist of two 4 GHz wide basebands (3 bit samplers) centered at 41.9 and 45.9 GHz, where each baseband was divided into 32 SPWs, each with a bandwidth of 128 MHz. The data were recorded in 64 unique SPWs, each comprised of 64 channels and each channel being 2 MHz wide, resulting in a total bandwidth of 8192 MHz (before "flagging"). The correlator setup for the observations of sources G35.20−0.74 and G45.47+0.05 was the same as that used at 1.3 cm, with the two basebands centered at 41.9 and 45.9 GHz. Source 3C48 was used as flux density and bandpass calibrator for regions AFGL 4029, AFGL 437, and NGC 7538 IRS9, and source 3C286 was used as flux density and bandpass calibrator for regions G35.20−0.74 and G45.47+0.05. For sources AFGL 4029 and AFGL 437, the observations were made alternating on a target source for ∼1.7 minutes and a phase calibrator for ∼1 minute, for a total on-source time of ∼7 minutes. For G35.20−0.74, the observations were made alternating on a target source for ∼2.5 minutes and a phase calibrator for ∼1 minute, for a total on-source time of ∼38 minutes. For G45.47+0.05, the observations were made alternating on a target source for ∼2 minutes and a phase calibrator for ∼1 minute, for a total on-source time of ∼23 minutes. For NGC 7538 IRS9, the observations were made alternating on a target source for ∼2 minutes and a phase calibrator for ∼1 minute, for a total on-source time of ∼11 minutes.

The data reduction was done in the same fashion as that for the 6 cm observations. In addition, we corrected for atmospheric opacity using the weather station information from the `plotWeather` task and creating the calibration table using `gencal`. The images were made using the `tclean` task and Briggs `Robust` = 0.5 weighting. For source G45.47+0.054, we performed self-calibration. We made two images, each of a ∼4 GHz baseband composed of 32 SPWs, and also a combined image using data from both basebands with a total of 64 SPWs. All maps were primary-beam-corrected. Columns 5 and 6 of Table 1 show the synthesized beam (size and position angle) and the rms of the combined images.

3. Theoretical Models

DLT17 investigated the protostellar properties of the eight SOMA sources presented in this paper, fitting the given set of infrared observations to the ZT model grid. However, the obtained properties of the IR-only SED models still have relatively large allowed variations in their parameters, i.e., significant degeneracies. In this paper, we aim to constrain the models further by comparing the radio observations and the TTZ16 model of free–free emission. In this section, we briefly revisit these theoretical models, i.e., the ZT and TTZ16 models, as well as the model selection methods.

3.1. ZT Model Grid for Dust Thermal Emission

In high-mass star formation, the vast majority of the energy emitted from the protostar and the innermost accretion flow is at optical and UV wavelengths. However, it is hard to directly detect the radiation from the protostar and its vicinity because

most of the flux emitted at those wavelengths is immediately absorbed by the surrounding material and reemitted in the infrared. Therefore, in order to investigate the properties of the embedded protostar, theoretical synthetic observational modeling is necessary. In a series of papers (Zhang & Tan 2011; Zhang et al. 2013, 2014; Zhang & Tan 2018), a theoretical model of the evolution of high-mass protostars based on the Turbulent Core scenario (McKee & Tan 2003) has been developed to provide the continuum flux at infrared and optical wavelengths. These are referred to as the ZT models.

In the ZT models, massive protostars are assumed to form from massive prestellar cores. The prestellar core properties are parameterized by the initial core mass M_c and the mass surface density of the ambient clump $\Sigma_{\rm cl}$. The latter determines the surface pressure of cores, and thus sets their sizes and densities together with M_c. The core undergoes collapse that forms a protostar-disk system at its center. The infalling structure is given by the self-similar solution (McLaughlin & Pudritz 1997) including effects of rotation (Ulrich 1976). The disk structure is described with an α-disk solution (Shakura & Sunyaev 1973), with an improved treatment including the infall to and outflow from the disk. The accretion rate onto the protostar is regulated by the feedback of the MHD disk wind (Blandford & Payne 1982; Matzner & McKee 2000). The protostellar evolution is calculated consistently with the accretion rate based on the method developed by Hosokawa & Omukai (2009) and Hosokawa et al. (2010), solving the basic stellar structure equations, i.e., continuity, hydrostatic balance, and energy conservation and transfer.

The evolution of the protostar and its surrounding gas structure are calculated self-consistently from the initial core parameters, i.e., M_c and $\Sigma_{\rm cl}$. The protostellar mass m_* is used as the third parameter to specify a particular stage of the evolutionary tracks. The continuum radiative transfer calculations at infrared and optical wavelengths have been performed for 432 physical models defined by different sets of (M_c, $\Sigma_{\rm cl}$, m_*) using the latest version of the Monte Carlo code, HOCHUNK3d (Whitney et al. 2003, 2013). For each model, 20 inclination angles $\theta_{\rm view}$ are sampled evenly in cosine space to produce the SEDs. To compare with the observations, a variable foreground extinction A_V is applied to the model SEDs. Thus, for a given source distance, a set of five parameters of (M_c, $\Sigma_{\rm cl}$, m_*, $\theta_{\rm view}$, A_V) gives one SED in the ZT model grid.

In DLT17, the authors searched for the best-fit models for the eight SOMA regions presented in this paper from the ZT model grid to investigate the properties of their protostars and surrounding gas. They used χ^2 minimization (in log space) to find the best models to fit a given set of observations at 8–70 μm for the eight SOMA sources. They successfully found models that can explain the infrared observed SED of each of these SOMA sources. However, even among the five best models, the obtained protostellar properties, such as stellar masses and bolometric luminosities, have relatively large degeneracies.

3.2. *TTZ16* Model for Free–Free Emission

To further constrain the protostellar properties, we use the additional diagnostic of free–free emission from photoionized gas. The UV flux dramatically increases during the Kelvin–Helmholtz contraction phase in the formation of a high-mass star, although this cannot be directly observed, due to absorption by the surrounding gas and dust. However, the gas absorbing Lyman continuum photons with >13.6 eV becomes ionized and emits thermal bremsstrahlung, i.e., free–free emission. Therefore, free–free emission at radio wavelengths from the photoionized region can provide the direct signpost of the evolutionary state of the embedded protostar.

Using the physical parameters of the best five models for the infrared, we calculated the photoionized structures and the free–free flux from them using the method of TTZ16. The basic protostellar properties and the density structure of the surrounding material are given from the ZT model grids. The ionizing photon rate is evaluated using the stellar atmosphere model of Castelli & Kurucz (2004). The temperature of the ionized gas is evaluated by CLOUDY (Ferland et al. 2013). The photoionized structure is obtained via the ray-tracing radiative transfer calculation (Stone et al. 1992; Tanaka et al. 2013), which allows a treatment of both the direct and diffuse ionizing radiation fields.

Some hydrodynamical simulations have included the MHD outflow feedback in high-mass star formation (e.g., Kuiper et al. 2016; Matsushita et al. 2017). In particular, Kuiper & Hosokawa (2018) recently performed the first simulations self-consistently including the protostellar outflow together with the radiation force and the photoionization feedback. However, because they focused on the dynamical impact of feedback processes, they have not conducted the observational modeling for dust and free–free emissions. Moreover, they explored only two initial conditions, while our semianalytic models span a wide range of environmental conditions (TTZ16; Tanaka et al. 2017). We note that the predictions of our semianalytic models, such as the star formation efficiencies, are quantitatively consistent with those from simulations by Kuiper & Hosokawa (2018), which supports the accuracy of our semianalytic models.

4. Results

In this paper, a radio detection is defined to occur when the peak intensity I_ν is $\geqslant$5 times the image rms (σ) in either of the baseband-combined images (see Section 2.1) at the different bands (i.e., *C*-, *K*-, or *Q*-band). For non-detections in one of the combined images, we report a 3σ limit value for the flux density at the given frequency. Figure 1 shows VLA contour plots of the *C*-band: 6 cm (red), *K*-band: 1.3 cm (magenta), and *Q*-band: 0.7 cm (blue) combined images for all the radio sources detected in our sample and overlaid to *SOFIA*-FORCAST 37μm images. The blue circles represent the SOMA aperture set from 70 μm images except for region IRAS 07299−1651, where the aperture radius is set from the 37.1 μm image) reported by DLT17 and used to build their IR SEDs (see Table 2 of DLT17). The infrared images presented in DLT17 (including *SOFIA*, *Herschel*, and *Spitzer* data) and the VLA data presented here have astrometric accuracies better than 0.″5 and 0.″1 (see Table 2), respectively.

Tables 3–10 report the radio parameters for each of the eight regions studied in this paper. These parameters were measured based on different size scales, as follows. The SOMA scale refers to the size of the aperture radius used by DLT17 to measure their IR fluxes (except for source AFGL 437; see below). The *Intermediate* scale is based on the morphology of the radio source, specifically whether the detections appear to be of jet-like nature. The *Inner* scale is given by the size of the central radio detection

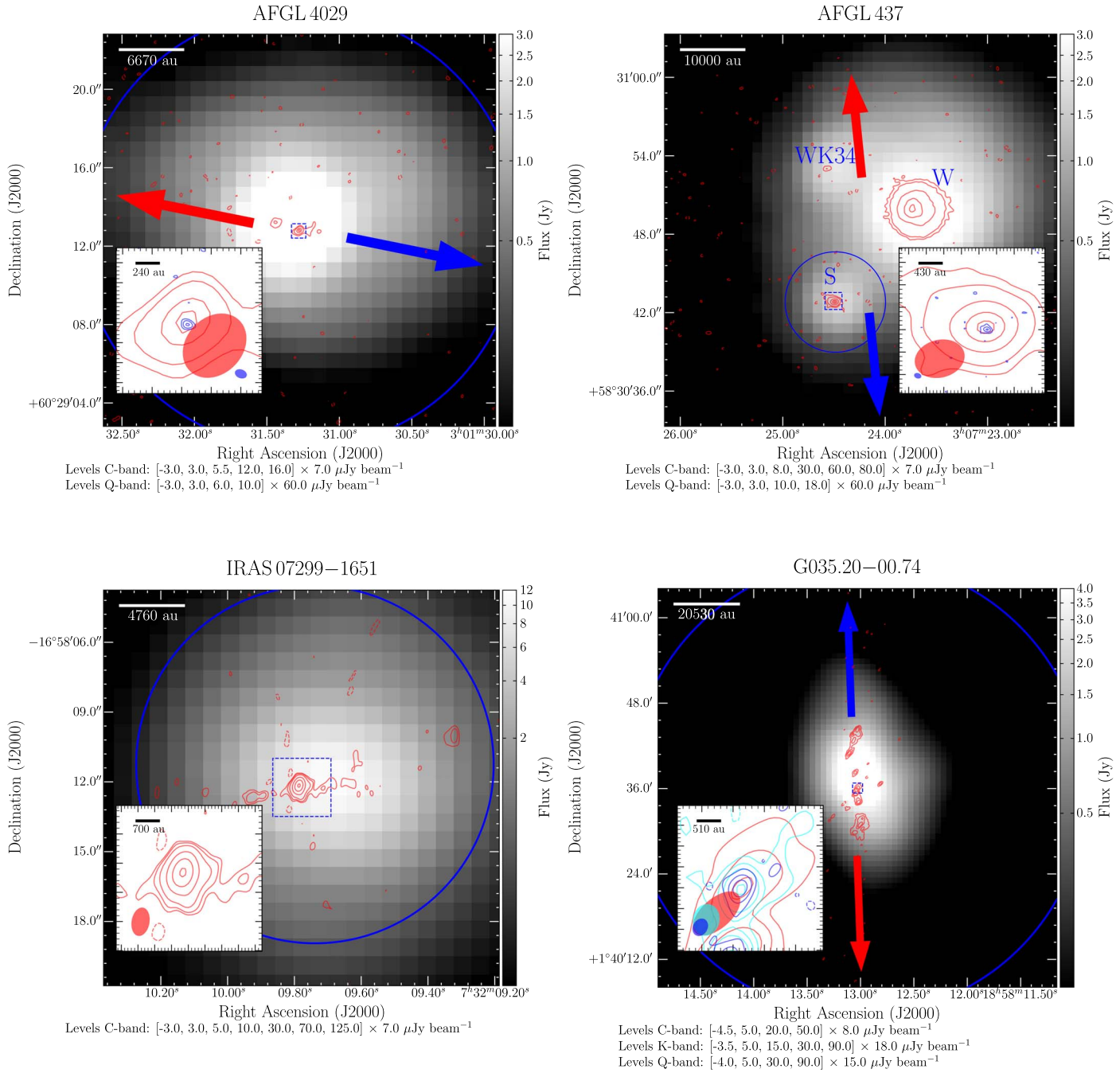

Figure 1. Images are SOFIA-FORCAST 37μm with VLA contours—red: *C*-band (6 cm); magenta: *K*-band (1.3 cm); blue: *Q*-band (0.7 cm)—of the combined radio maps overlaid. Contours in Cepheus A are 8.3 GHz and 42.9 GHz from Curiel et al. (2006); see their Figure 2 for a higher-resolution image of these contours. The location and size of this inset are represented by the small blue box superimposed over the region. The dashed squares correspond to the area of the inset image showing a zoom-in of the central region, and the synthesized beams are shown in the lower corners of these insets. The blue circles are the SOMA apertures used by DLT17 and reported in their Table 2. The aperture radius is defined from 70 μm emission, except for IRAS 07299−1651 where it is set at 37.1 μm). The blue and red arrows represent the direction of a molecular outflow detected toward the region. A scale bar in units of au is shown in the upper left of the figures.

that is likely most closely associated with the driving protostar (i.e., association with compact millimeter dust continuum emission). For the VLA data presented, we determined the flux density S_ν in each wideband image in the SOMA and *Intermediate* scales by using the task `imstat` of CASA, either enclosing the SOMA aperture in a circular region or enclosing the elongated jet-like structure in a box, respectively (see Table 11). The uncertainties of the flux density for these two scales are estimated as $\sigma_{\rm image}(\rm npts/beam\ area)^{0.5}$ added in quadrature with an assumed 10% error in calibration, where $\sigma_{\rm image}$ is the rms of the image, *npts* is the number of pixels enclosed in the box or the circular region, and the *beam area* is the number of pixels within a synthesized beam of the image. For the *Inner* scale, we determined the flux density using the task `imfit` of CASA, and the uncertainty was estimated using the statistical error from the Gaussian fit added in quadrature with an assumed 10% error in calibration.

Column 1 of Tables 3–10 shows the given scale; for each scale, columns 2 and 3 report the R.A. and decl. For the SOMA scale, these refer to the pointing center observations of *SOFIA*-

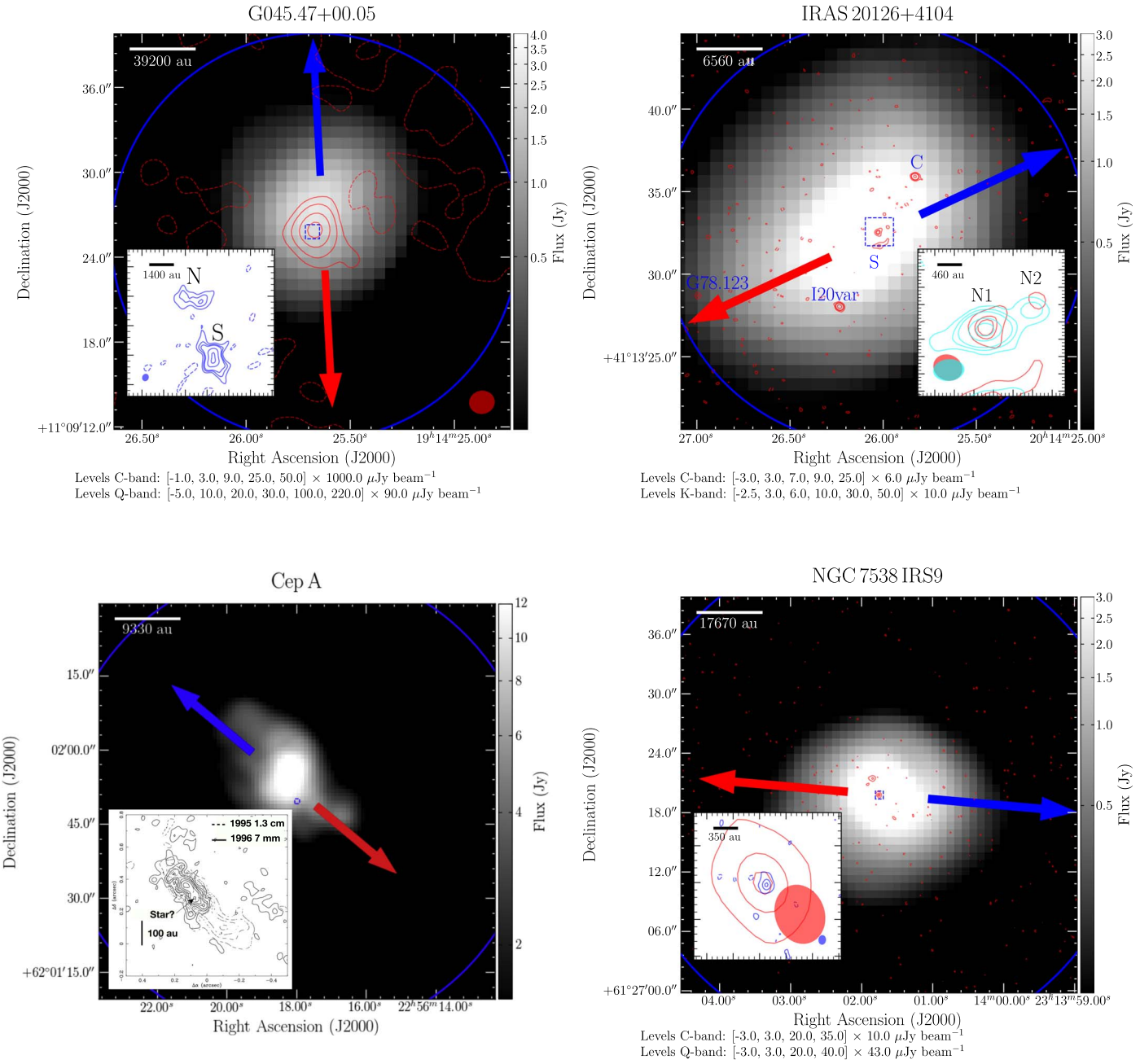

Figure 1. (Continued.)

FORECAST (see DLT17 Table 1); for the *Intermediate* scale, they refer to a middle point in the jet-like detection; and for the *Inner* scale, they refer to the R.A. and decl. of the peak intensity of the central detected object. The following columns are the flux densities (S_ν) at different frequencies, with the uncertainties given in parentheses, and the last columns in Tables 3–10 report the spectral indices and their uncertainties at each scale (see Section 4.2). Because the radio data are not sensitive to extended emission over scales as large as the SOMA and possibly the *Intermediate* scales, the flux measurements represent the sum over all compact sources within the scale, and the spectral indices contain some corresponding uncertainty. The error bars for these measurements are large, due to having many independent beams within the scale.

4.1. Morphology and Multiplicity

All the target regions presented in this paper have been detected in the cm continuum; we describe their morphology as compact if the detection shows no structure on the scale of a few synthesized beams, or extended otherwise. Below, we describe the centimeter wavelength detections toward each target; for a detailed background on each of these regions, see DLT17.

4.1.1. AFGL 4029

AFGL 4029 is composed of two mid-IR sources, IRS1 and IRS2, with the former being the source of interest in this work. In our data, we detected at least four centimeter continuum sources at *C*-band and one at *Q*-band, with the eastern and

Table 3
AFGL 4029: Parameters from Radio Continuum

Scale	R.A. (J2000)	Decl. (J2000)	$S_{5.3\ \mathrm{GHz}}$ (mJy)	$S_{6.3\ \mathrm{GHz}}$ (mJy)	$S_{41.9\ \mathrm{GHz}}$ (mJy)	$S_{45.9\ \mathrm{GHz}}$ (mJy)	Spectral Index
SOMA	03:01:31.28	+60.29.12.9	0.44(0.52)	0.42(0.77)	4.73(30.04)	<134.24	<1.1
Intermediate	03:01:31.28	+60.29.12.9	0.31(0.06)	0.34(0.08)	0.95(3.12)	<14.10	<0.5
Inner	03:01:31.28	+60:29:12.8	0.14(0.02)	0.16(0.03)	0.74(0.11)	0.48(0.11)	0.7(0.1)

Note. The *Intermediate* scale corresponds to the extent of the radio jet. Units of R.A. are hours, minutes, and seconds. Units of decl. are degrees, arcminutes, and arcseconds.

Table 4
AFGL 437: Parameters from Radio Continuum

Scale	R.A. (J2000)	Decl. (J2000)	$S_{5.3\ \mathrm{GHz}}$ (mJy)	$S_{6.3\ \mathrm{GHz}}$ (mJy)	$S_{41.9\ \mathrm{GHz}}$ (mJy)	$S_{45.9\ \mathrm{GHz}}$ (mJy)	Spectral Index
SOMA	03:07:24.49	+58.30.42.8	0.82(0.28)	0.36(0.57)	0.28(10.34)	3.37(15.54)	−4.7(3.6)
Intermediate	…	…	…	…	…	…	…
Inner	03:07:24.49	+58:30:42.8	0.77(0.09)	0.80(0.09)	1.39(0.20)	1.57(0.30)	0.3(0.1)

Note. Units of R.A. are hours, minutes, and seconds. Units of decl. are degrees, arcminutes, and arcseconds.

Table 5
IRAS 07299−1651: Parameters from Radio Continuum

Scale	R.A. (J2000)	Decl. (J2000)	$S_{5.0\ \mathrm{GHz}}$ (mJy)	$S_{7.0\ \mathrm{GHz}}$ (mJy)	Spectral Index
SOMA	07:32:09.74	−16.58.11.3	1.56(0.25)	1.62(0.34)	0.1(0.8)
Intermediate	…	…	…	…	…
Inner	07:32:09.79	−16:58:10.9	1.15(0.12)	1.47(0.16)	0.7(0.5)

Note. Units of R.A. are hours, minutes, and seconds. Units of decl. are degrees, arcminutes, and arcseconds.

Table 6
G35.20-0.74: Parameters from Radio Continuum

Scale	R.A. (J2000)	Decl. (J2000)	$S_{4.9\ \mathrm{GHz}}$ (mJy)	$S_{6.9\ \mathrm{GHz}}$ (mJy)	$S_{19.9\ \mathrm{GHz}}$ (mJy)	$S_{23.9\ \mathrm{GHz}}$ (mJy)	$S_{41.9\ \mathrm{GHz}}$ (mJy)	$S_{45.9\ \mathrm{GHz}}$ (mJy)	Spectral Index
SOMA	18:58:13.02	+01.40.36.2	15.08(1.77)	13.51(1.77)	11.73(5.32)	13.43(8.85)	10.80(13.97)	5.68(25.52)	−0.2(0.3)
Intermediate	18:58:13.02	+01.40.36.2	14.46(1.45)	12.88(1.30)	14.53(1.52)	15.15(1.65)	7.05(1.09)	6.22(1.49)	−0.2(0.1)
Inner	18:58:13.04	+01:40:35.9	0.74(0.12)	0.79(0.10)	1.82(0.21)	2.27(0.26)	2.52(0.26)	3.08(0.32)	0.7(0.1)

Note. The *Intermediate* scale corresponds to the extent of the radio jet. Units of R.A. are hours, minutes, and seconds. Units of decl. are degrees, arcminutes, and arcseconds.

Table 7
G45.47+0.05: Parameters from Radio Continuum

Scale	R.A. (J2000)	Decl. (J2000)	$S_{5\ \mathrm{GHz}}$ (mJy)	$S_{41.9\ \mathrm{GHz}}$ (mJy)	$S_{45.9\ \mathrm{GHz}}$ (mJy)	Spectral Index
SOMA	19:14:25.67	+11.09.25.4	58.00(13.52)	140.10(45.80)	157.21(78.91)	0.4(0.2)
Intermediate	…	…	…	…	…	…
Inner	19:14:25.67	+11:09:25.9	91.00(9.75)	102.90(11.27)	119.70(13.05)	0.1(0.1)

Note. The quoted flux at 5 GHz is from Urquhart et al. (2009). The quoted fluxes at the *Inner* scale for the higher frequencies correspond to the southern source. Units of R.A. are hours, minutes, and seconds. Units of decl. are degrees, arcminutes, and arcseconds.

central sources being 5σ detections (also reported by Zapata et al. 2001) and the two western ones being 3σ detections. We detected only one of the sources of the binary system found by Zapata et al. (2001) at 3.6 cm (which they named G138.295 +1.555 S and located at R.A.(J2000) = $03^{h}01^{m}31\overset{s}{.}273$, decl. (J2000) = $+60°29'12\overset{''}{.}80$) even though our observations have ∼2 times higher sensitivity and a resolution (∼$0\overset{''}{.}3$) similar to theirs. This may be further indication that source G138.295 +1.555 N (not detected in our analyzed data), which they reported to be at a separation of ∼$0\overset{''}{.}6$ (or 1200 au at the

Table 8
IRAS 20126+4104: Parameters from Radio Continuum

Scale	R.A. (J2000)	Decl. (J2000)	$S_{4.9\ \mathrm{GHz}}$ (mJy)	$S_{7.4\ \mathrm{GHz}}$ (mJy)	$S_{20.9\ \mathrm{GHz}}$ (mJy)	$S_{25.5\ \mathrm{GHz}}$ (mJy)	Spectral Index
SOMA	20:14:26.05	+41.13.32.5	0.37(0.54)	0.50(0.75)	0.29(1.49)	1.13(2.76)	0.2(1.9)
Intermediate	...	...	...	...	...	...	...
Inner	20:14:26.03	+41:13:32.5	0.06(0.02)	0.08(0.02)	0.64(0.07)	0.85(0.09)	1.8(0.1)

Note. Units of R.A. are hours, minutes, and seconds. Units of decl. are degrees, arcminutes, and arcseconds.

Table 9
Cepheus A: Parameters from Radio Continuum

Scale	R.A. (J2000)	Decl. (J2000)	$S_{1.5\ \mathrm{GHz}}$ (mJy)	$S_{4.9\ \mathrm{GHz}}$ (mJy)	$S_{8.3\ \mathrm{GHz}}$ (mJy)	$S_{14.9\ \mathrm{GHz}}$ (mJy)	$S_{23.1\ \mathrm{GHz}}$ (mJy)	$S_{43.0\ \mathrm{GHz}}$ (mJy)	Spectral Index
SOMA	...	...	...	...	...	...	...	...	...
Intermediate	22:56:17.98	+62.01.49.4	3.40(0.10)	7.50(0.10)	9.80(0.10)	15.80(0.20)	...	*35.00(2.00)*	*0.66(0.01)*
Inner	22:56:17.99	+62:01:49.6	...	...	6.85(0.07)	...	18.50(0.30)	65.00(0.50)	1.38(0.01)

Note. The parameters shown in the table are from Rodriguez et al. (1994) and Curiel et al. (2006) for the *Intermediate* and the *Inner* scale, respectively. Units of R.A. are hours, minutes, and seconds. Units of decl. are degrees, arcminutes, and arcseconds.

Table 10
NGC 7538 IRS9: Parameters from Radio Continuum

Scale	R.A. (J2000)	Decl. (J2000)	$S_{5.3\ \mathrm{GHz}}$ (mJy)	$S_{6.3\ \mathrm{GHz}}$ (mJy)	$S_{41.9\ \mathrm{GHz}}$ (mJy)	$S_{45.9\ \mathrm{GHz}}$ (mJy)	Spectral Index
SOMA	23:14:01.77	+61.27.19.8	5.00(1.68)	25.74(5.46)	2.47(103.89)	<515.49	<1.1
Intermediate	...	...	...	...	...	...	...
Inner	23:14:01.76	+61:27:19.8	0.42(0.04)	0.48(0.06)	2.50(0.29)	2.47(0.29)	0.8(0.1)

Note. Units of R.A. are hours, minutes, and seconds. Units of decl. are degrees, arcminutes, and arcseconds.

distance of the region) from G138.295+1.555 S, is a variable radio source, as also suggested by Zapata et al. (2001).

Moreover, we detected the fainter, extended east–west emission that they interpreted as being part of an ionized jet that is emanating from G138.295+1.555 S (our detected radio source at the *Inner* scale) based on the morphology and their alignment with larger-scale outflows, e.g., optical jet (Ray et al. 1990) and CO molecular outflow (Ginsburg et al. 2011). Zapata et al. (2001) reported a flux density of ∼0.25 mJy at 3.6 cm for G138.295+1.555 S and detected it as an unresolved source at a resolution of ∼0.″3. The presented data provide further evidence that this system corresponds to an ionized jet (with a projected length of ∼5000 au) based on the morphology, weak cm continuum emission, and a spectral index $\alpha \sim 0.7$, which is consistent with the typical spectral index of ionized jets (e.g., Reynolds 1986; Anglada et al. 1998; TTZ16). Additionally, although the three other components of the jet (eastern and western components) are not detected at *Q*-band, probably due to a lack of sensitivity at that band, our upper limit estimates of their spectral indices ($\alpha \lesssim 1$) are still consistent with the expected values for ionized jets.

4.1.2. AFGL 437

AFGL 437 is an infrared star-forming region composed of at least four IR sources (e.g., Wynn-Williams et al. 1981), where sources AFGL 437W and AFGL 437S have been the only ones reported to be associated with centimeter continuum emission. In our study of this region, AFGL 437W and AFGL 437S are detected at $>5\sigma$ as extended and compact radio sources, respectively. Also, for the first time (to the knowledge of the authors), we detected very compact and unresolved centimeter continuum emission from the very embedded IR source WK 34, which is associated with AFGL 437N. The position of its peak intensity.″ is R.A.(J2000) = $03^{h}07^{m}24.^{s}571$, decl.(J2000) = +58° 30′53.″00. WK 34 is very weak at 5.8 GHz, with a flux density of ∼60 μJy, but it has a flux density of ∼700 μJy at 44GHz, giving a positive spectral index of ∼1.2. Weintraub & Kastner (1996) speculated that WK 34 is tracing an outflow cavity and Kumar Dewangan & Anandarao (2010) suggested that WK 34 is a high-mass protostar at an earlier stage than AFGL 437W and AFGL 437S. Therefore, our high-sensitivity observations provide further evidence that high-mass stars, even at the earlier stages, are associated with very weak thermal radio continuum emission likely associated with ionized jets.

Moreover, a CO molecular outflow roughly oriented N-S has been reported (Gomez et al. 1992; Qin et al. 2008) toward the center of the IR-emitting region, but it has a very low degree of collimation, perhaps due to the superposition of multiple unresolved outflows (Manjarrez et al. 2012). AFGL 437W and AFGL 437S have previously been observed at 3.6 cm and 2 cm using the VLA by Torrelles et al. (1992) and Manjarrez et al. (2012), with angular resolutions of ∼4″ and ∼1″, respectively. AFGL 437W is a resolved extended source with estimated total flux densities of ∼18 mJy at 3.6 cm and ∼17 mJy at 2 cm, and of ∼22 mJy at 3.6 cm and ∼28 mJy at 2 cm, from

Table 11
SOMA and *Intermediate* Scales

Region	SOMA R ($''$)	*Intermediate* $w('') \times h(''$)
AFGL 4029	11.2	3.37 × 1.27
AFGL 437	3.84	⋯
IRAS 07299−1651	7.7	⋯
G35.20−0.74	32.0	3.36 × 16.15
G45.47+0.05	14.4	⋯
IRAS 20126+4104	12.8	⋯
Cepheus A	48.0	⋯[a]
NGC 7538 IRS9	25.6	⋯

Note. The reported values correspond to a circle of radius R for the SOMA scale and a box of height h and width w for the *Intermediate* scale.
[a] Size changes with frequency, and they are reported in Rodriguez et al. (1994) Table 1.

Table 12
AFGL 437S: Infrared Flux Densities

Facility	λ (μm)	F_{λ,b_sub}[a] (Jy)	F_{λ}[a] (Jy)
Spitzer/IRAC	3.6	0.35	0.40
Spitzer/IRAC	4.5	0.71	0.78
Spitzer/IRAC	5.8	1.56	1.77
SOFIA/FORCAST	7.7	3.13	3.89
Spitzer/IRAC	8.0	2.77	3.32
SOFIA/FORCAST	19.7	22.37	27.09
SOFIA/FORCAST	31.5	46.27	65.10
SOFIA/FORCAST	37.1	53.79	76.69

Note. Here, F_{λ,b_sub} and F_{λ} correspond to the flux density derived with and without background subtraction, respectively.
[a] Flux density derived with a fixed aperture radius of $R_{ap} = 3\farcs84$ from the 70 μm data.

Torrelles et al. (1992) and Manjarrez et al. (2012), respectively. AFGL 437W appears to be an optically thin UC H II region likely ionized by an early B-type zero-age main sequence (ZAMS) star (Torrelles et al. 1992), although Manjarrez et al. (2012) suggested that this source is a radio jet, based on their detected morphology at 2 cm. Because AFGL 437W is resolved and extended, the archival data at 6 cm is missing part of its flux, and the higher resolution data at 0.7 cm are also resolving out this source.

Torrelles et al. (1992) and Manjarrez et al. (2012) estimated a total flux density for AFGL 437S of ∼1 mJy at 3.6 cm and 2 cm, ∼1.5 mJy at 3.6 cm, and <2 mJy at 2 cm, respectively. In our data, AFGL 437S appears to be slightly elongated in the NE-SW direction at longer wavelengths, and it has a rising spectral index, consistent with Manjarrez et al. (2012). Thus, AFGL 437S could be either an optically thick UC/HC H II region or an ionized jet. In this study, we test the scenario that AFGL 437S is associated with an ionized jet that is likely undergoing mass loss (Manjarrez et al. 2012). In order to do so, we have built the SED for AFGL 437S, and therefore we do not use the photometry measured by DLT17, whose SED includes emission from all the four IR sources of the cluster. Our SOMA scale for AFGL 437S has a circular aperture of radius $R_{ap} = 3\farcs84$ around AFGL 437S, and we only use the data at wavelengths <40 μm because the source is unresolved at longer wavelengths. Table 12 has the integrated flux densities for AFGL 437S from the IR data, and Table 4 shows our measured total flux density for the centimeter wavelengths archival data.

4.1.3. IRAS 07299−1651

IRAS 07299−1651 appears extended in the NIR and MIR; it is associated with methanol maser emission that shows a velocity gradient and evidence of CO outflow wings, and all these tracers share a similar elongation axis in the NW-SE direction (Walsh et al. 1999, 2001).

We present 6 cm observations of this region where we have detected at least one resolved and slightly elongated source. In addition, we detect at least two more unresolved sources that appear aligned with the central source in the E-W direction. However, our resulting images of this region have calibration errors and the source is very faint for self-calibration, so we can not rule out the possibility that these two sources are image artifacts. The central detection is consistent with the source reported by Walsh et al. (1998) within their absolute positional accuracy (∼1$\farcs$0), and they reported that it is associated with 6.7 GHz methanol masers. At this point, the nature of IRAS 07299−1651 is unclear: it could be either an UC/HC H II region or an ionized jet. Thus, we require additional information, such as high-resolution centimeter continuum at higher frequencies, to further constrain its nature.

4.1.4. G35.20−0.74

Also known as G35.20−0.74N, this region is seen in the infrared as an elongated source oriented N-S that hosts a weakly collimated bipolar CO molecular outflow that extends in the NE-SW direction. This region is associated with at least three HMCs, labeled A, B, and C, which are oriented in the NW-SE direction (Sánchez-Monge et al. 2014). Centimeter continuum observations (e.g., Gibb et al. 2003) have revealed the presence of a string of radio sources that are coincident with the N-S elongated IR emission seen in the region. Recently, Beltrán et al. (2016) detected 17 cm continuum sources at angular resolutions of ∼0$\farcs$4– ∼0$\farcs$05 (some of these data are also used in our study) toward G35.20−0.74; based on the spectral indices of each component, they found that core B is associated with an UC/HC H II region (their source 8a) that is part of a young binary system (∼0$\farcs$37 apart), and it is likely driving an ionized jet oriented N-S (with a projected length of ∼33,000 au). Beltrán et al. (2016) proposed that most of the radio sources detected are part of the ionized jet and that, based on their spectral indices, some of the emission of these knots is non-thermal. The ionized jet is expanding at a velocity of ∼300 km s^{-1}, and it appears to be precessing as suggested by its S-shaped morphology and the misalignment with respect to the larger-scale CO molecular outflow (Beltrán et al. 2016). Cores A and C are also associated with UC/HC H II regions and are within our SOMA scale, hence the higher flux densities measured at this scale. However, we also measure a high flux density at our *Intermediate* scale compared with the *Inner* scale.

4.1.5. G45.47+00.05

G45.47+00.05 appears as a resolved and slightly elongated radio continuum source (e.g., Urquhart et al. 2009; Towner et al. 2017), associated with at least one molecular outflow roughly oriented with a N-S axis (Wilner et al. 1996). Wood & Churchwell (1989) observed this source at 6 cm with an angular

resolution of ∼0.″4 and cataloged it as an irregular UC H II region because their observations revealed a NE-SW elongation as well as a slight NW-SE elongation. Wilner et al. (1996) studied the centimeter continuum spectrum of G45.47+00.05 and suggested that it was consistent with a partially ionized stellar wind. Towner et al. (2017) presented additional VLA 1.3 cm observations estimating a flux density of ∼180 mJy with an angular resolution of ∼1″ that also revealed an elongated morphology along the NW-SE axis, suggesting an ionized jet nature. In this work, we present very high-resolution (∼0.″04) VLA *Q*-band archival data where we can see for the first time (to the knowledge of the authors) that G45.47+00.05 is fragmented into at least two centimeter continuum sources ∼0.″4 apart (or ∼3400 au at the distance of G45.47+00.05). The southern source, which we have named G45.47+00.05S, is very bright at 43.9 GHz, with a flux density of ∼110 mJy; it appears slightly elongated along the N-S axis, and its peak intensity position at that frequency is R.A.(J2000) = $19^{h}14^{m}25^{s}.677$, decl.(J2000) = +11°09′25.″56. The northern source, which we have named G45.47+00.05N, is weaker at 43.9 GHz, with a flux density of ∼20 mJy; it has a jet-like morphology elongated in the E-W axis, and its peak intensity position at that frequency is R.A.(J2000) = $19^{h}14^{m}25^{s}.683$, decl. (J2000) = +11°09′25.″96. Our *Inner* scale is centered around G45.47+00.05S at the *Q*-band, where the source is resolved.

4.1.6. IRAS 20126+4104

IRAS 20126+4104 has infrared emission that is slightly elongated along the same NW-SE axis as the associated bipolar molecular outflow (e.g., Cesaroni et al. 1997). Rosero et al. (2016) detected at least five centimeter continuum sources that are within our SOMA aperture, as seen in Figure 1. Hofner et al. (2007) suggested that the central, slightly elongated sources seen in Figure 1 correspond to two collimated ionized jets, one of them composed of radio sources N1 and N2 and the second ionized jet known as source S. It has been suggested that source N1 sits at the origin of the larger-scale molecular outflow; it also appears to be surrounded by a nearly Keplerian and stable accretion disk (e.g., Cesaroni et al. 2014; Chen et al. 2016). Additionally, Hofner et al. (2007) reported that the southern radio source toward IRAS 20126+4104 (labeled I20var) is a variable radio source, consistent with gyrosynchrotron emission from a T-Tauri star. I20var is located ∼5.″0 to the SE of source N1. The other two sources found by Rosero et al. (2016) were labeled source C (located ∼4.″0 NW apart from N1) and G78.123+3.629 (located ∼11.″5 SE apart from N1, very close to the edge of the millimeter dust core). These are new detections with reported spectral indices that are consistent with non-thermal emission. It is possible that, at the distance of IRAS 20126+4104, the VLA could still detect low-mass stars (V. Rosero et al. 2019, ApJ, submitted), so these non-thermal, highly variable radio sources could be flaring T-Tauri stars. In this scenario, IRAS 20126+4104 would be a small multiple system of two high-mass protostars surrounded by at least three pre-main sequence low-mass stars. The four central sources are within a projected radius of ∼4.″5 (7400 au at the distance of IRAS 20126+4104).

4.1.7. Cepheus A

Cepheus A is a well-known star-forming region, seen in the infrared as an elongated source oriented NE-SW. This region is the host of a complex multipolar CO molecular outflow that is likely powered by a small cluster of deeply embedded protostars (e.g., Curiel et al. 2006; Zapata et al. 2013). Our SOMA aperture encloses the whole Cepheus A East region, which is composed of several centimeter continuum sources as seen in Zapata et al. (2013). The brighter centimeter continuum source found toward this region, known as HW2, is an ionized thermal jet oriented NE-SW; it is thought to be the main driver of the complex outflow activity in Cepheus A and to contribute at least half of the total luminosity of the region (e.g., Zapata et al. 2013). In addition, the ionized jet in HW2 is associated and aligned with a bipolar HCO^{+} molecular outflow (Gómez et al. 1999). Curiel et al. (2006) resolved the Cepheus A HW2 ionized jet at 3.6 cm in three radio sources, where HW2 is the central powering source and the NE and SW sources are knots along the jet that are moving away from HW2 at a velocity of ∼500 km s^{-1}. Based on maser and millimeter observations, some authors have suggested that HW2 has an associated circumstellar disk (e.g., Patel et al. 2005; Sugiyama et al. 2014; Sanna et al. 2017). We used the reported values from Curiel et al. (2006) with angular resolutions of ∼0.″27 and ∼0.″05 for the central source for our study of the *Inner* scale. We used the reported values from Rodriguez et al. (1994) of the radio jet for our study of the *Intermediate* scale. We are not analyzing the SOMA aperture toward this region, due to a lack of a complete suit of observations that enclosed all the radio sources at this scale.

4.1.8. NGC 7538 IRS9

NGC 7538 IRS9 is part of a cluster of infrared regions that host several high-mass star-forming cores. Sandell et al. (2005) detected a faint and marginally resolved radio source (known as IRS 9) in this region using VLA data at angular resolution of ∼1″ at 3.6 cm and 6 cm, and with rms noise of 60 μJy $beam^{-1}$ and 100 μJy $beam^{-1}$, respectively. Based on their measured spectral index, they have suggested that IRS 9 is free–free emission from an ionized jet, a scenario that is consistent with the observed collimated, compact, and bipolar HCO^{+} molecular outflow that is centered on IRS 9 and oriented E-W. Using VLA data at 43.3 GHz, van der Tak & Menten (2005) detected IRS 9 at two angular resolutions of ∼0.″5 and ∼0.″05. Our results show further evidence that the radio emission from IRS 9 is dominated by free–free emission. Additionally, these archival observations have allowed us to detect a new weak and unresolved radio source at 5.8 GHz, located ∼1.″8 NE from IRS9 (or ∼4800 au). This new radio detection has a flux density at 5.8 GHz of ∼0.2 mJy, and its peak intensity position is R.A.(J2000) = $23^{h}14^{m}01^{s}.844$, decl.(J2000) = +61°27′21.″46. This source appears to be undetected by the observations of Sandell et al. (2005), which suggests that this newly detected radio source may be a radio variable source or that their observations lacked the angular resolution to distinguish these two sources. We estimate an upper limit on the radio spectrum for this new component that is consistent with a flat or even a negative spectral index.

4.2. Radio SEDs

In Figure 2, we present the centimeter SEDs for our regions. The dashed lines are the best fit to the data of a power law of the form $S_{\nu} \propto \nu^{\alpha}$, where α is the spectral index, derived at the different scales: "*SOMA*," "*Intermediate*," and "*Inner*," as described above. The spectral index was calculated using the

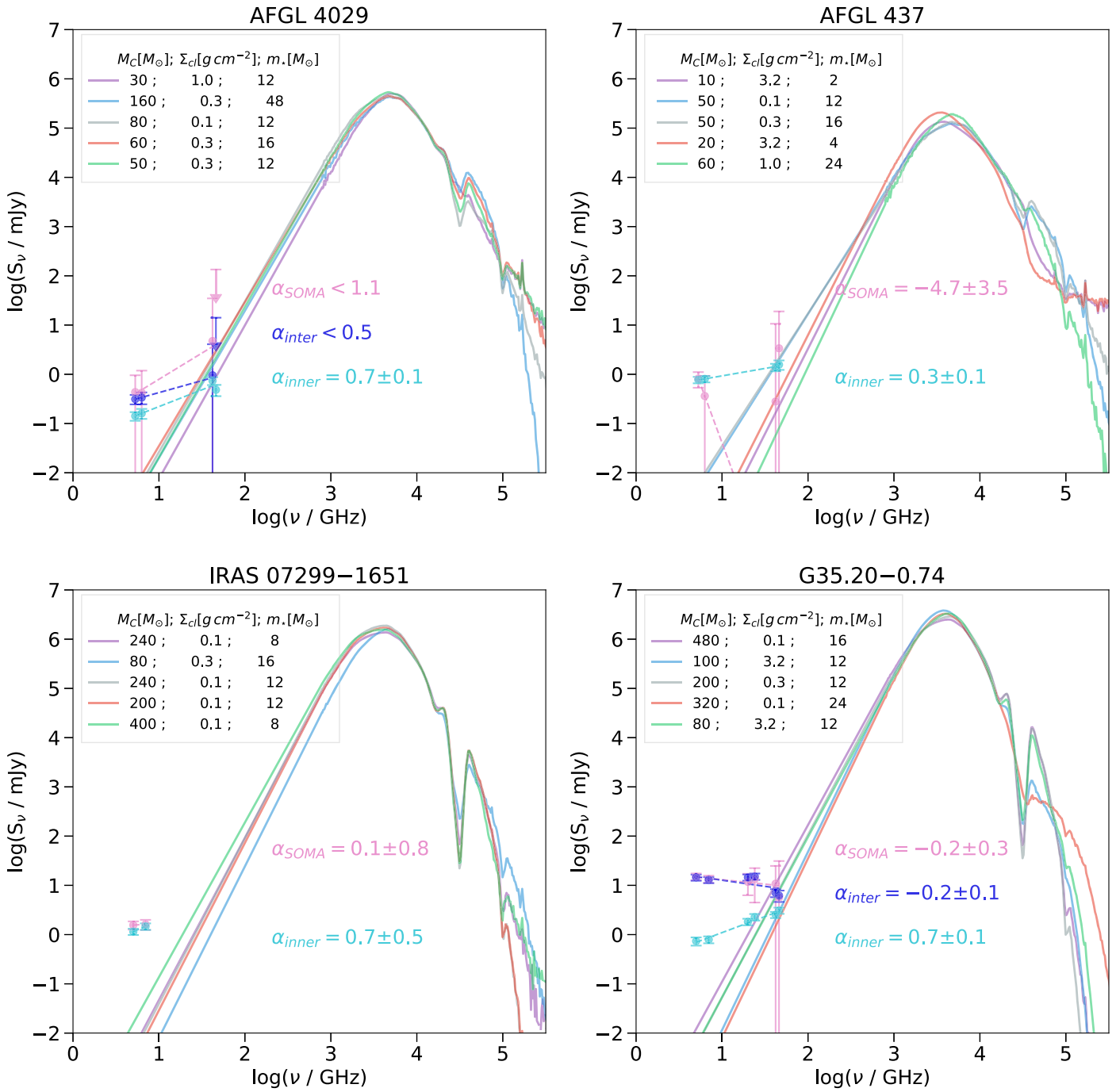

Figure 2. Observed radio spectral energy distributions of SOMA protostars. The circles correspond to the flux density as a function of frequency for each scale (magenta: SOMA; blue: *Intermediate*; cyan: *Inner*). Error bars are explained in Section 4.2. The dashed lines are the best fit to the data from a power law of the form $S_\nu \propto \nu^\alpha$. The solid lines show the five best IR SED ZT models as fit by DLT17 (see legend).

flux density at the central frequencies from the images (and/or the available data in the literature), so α is calculated over a wide frequency range (>20 GHz), except for IRAS 07299 −1651 where we only have data at 6 cm. The presented archival data were observed at different angular resolutions at different frequencies, with the lower frequency observed (*C*-band: 6 cm) at a resolution around 10 times lower than the higher frequency (*Q*-band: 0.7 cm). This is not a major concern for sources measured to be very compact or unresolved at *C*-band because they will then be smaller than the largest angular scale for which the *Q*-band observations are sensitive. For the sources in this study (typically at about 2 kpc), this corresponds to a linear size of ∼2400 au.

However, more extended sources may suffer from resolution bias and/or lack of short spacing data (resolved out), affecting our ability to recover a source's entire flux. Additionally, at the higher frequencies (*K*-band and *Q*-band in our study) the fluxes are most likely measuring the combination of dust and free–free emission (see Brogan et al. 2016). We assume that the fluxes at *Q*-band are an upper limit on the free–free emission contribution. The uncertainty in the spectral index was calculated with a Monte Carlo simulation that bootstrapped

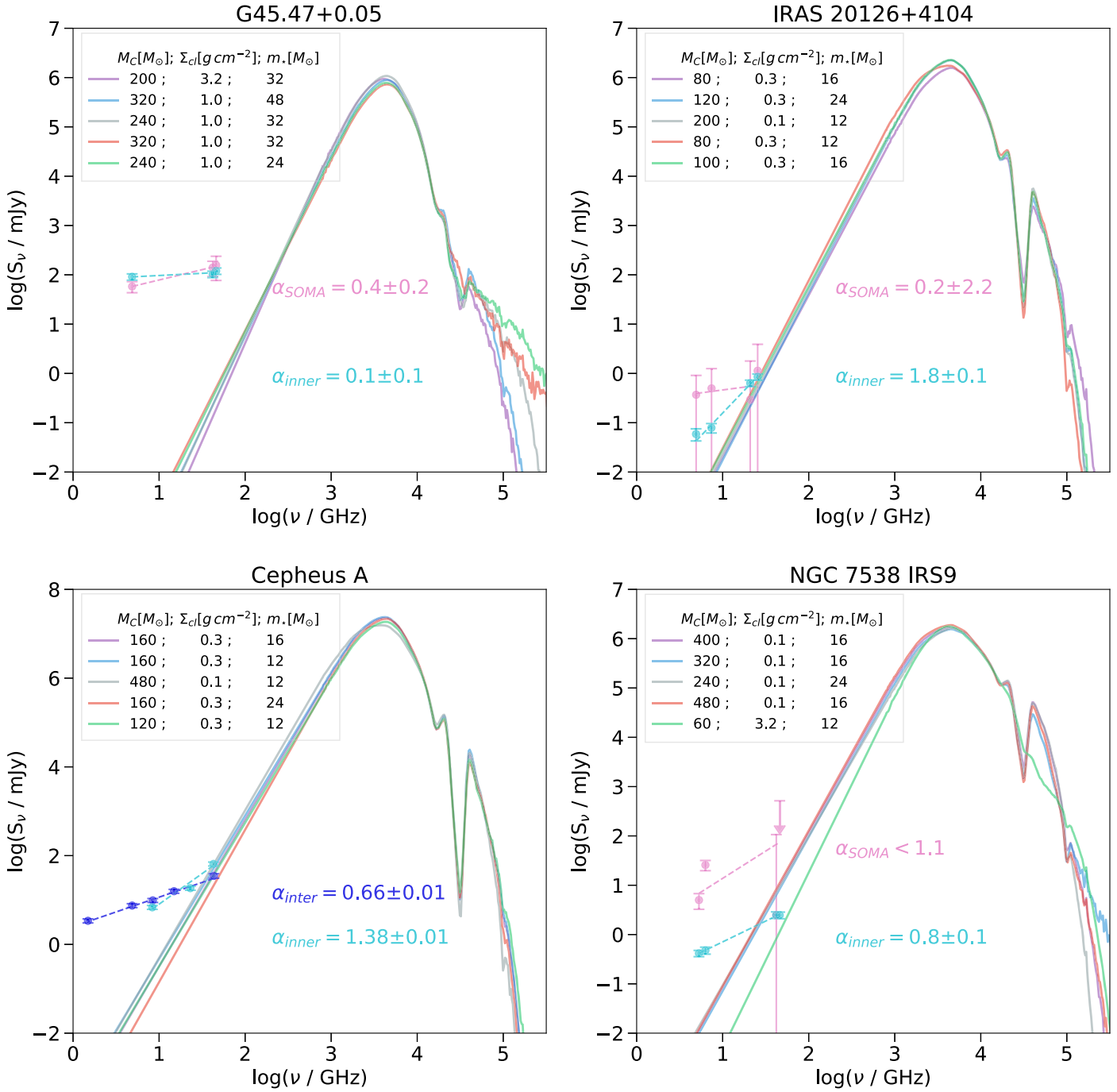

Figure 2. (Continued.)

the flux density uncertainties. We estimated an upper limit in the spectral index for nondetections at higher frequencies using a value of S_ν of 3σ.

5. Analysis

The centimeter continuum emission associated with the regions located at distances >1 kpc have low radio fluxes (<3 mJy) in our *Inner* scale, except for G45.47+0.05. The analyzed data do not allow us to make a systematic study of the nature of this detected emission, but we favor the speculation from previous studies that some of them are part of a protostellar jet/wind, at least based on their morphology, as in the case of AFGL 4029, G35.20−0.74, IRAS 20126+4104. Cepheus A is the only region in this study located at a distance <1 kpc, and it is one of the best examples of a collimated ionized jet from a high-mass protostar in the literature (Rodriguez et al. 1994).

Figure 3 shows the extended SEDs, i.e., including radio fluxes as well as the infrared fluxes from DLT17, for our eight sources. The solid colored lines (except yellow ones) correspond to the best five models obtained from the ZT

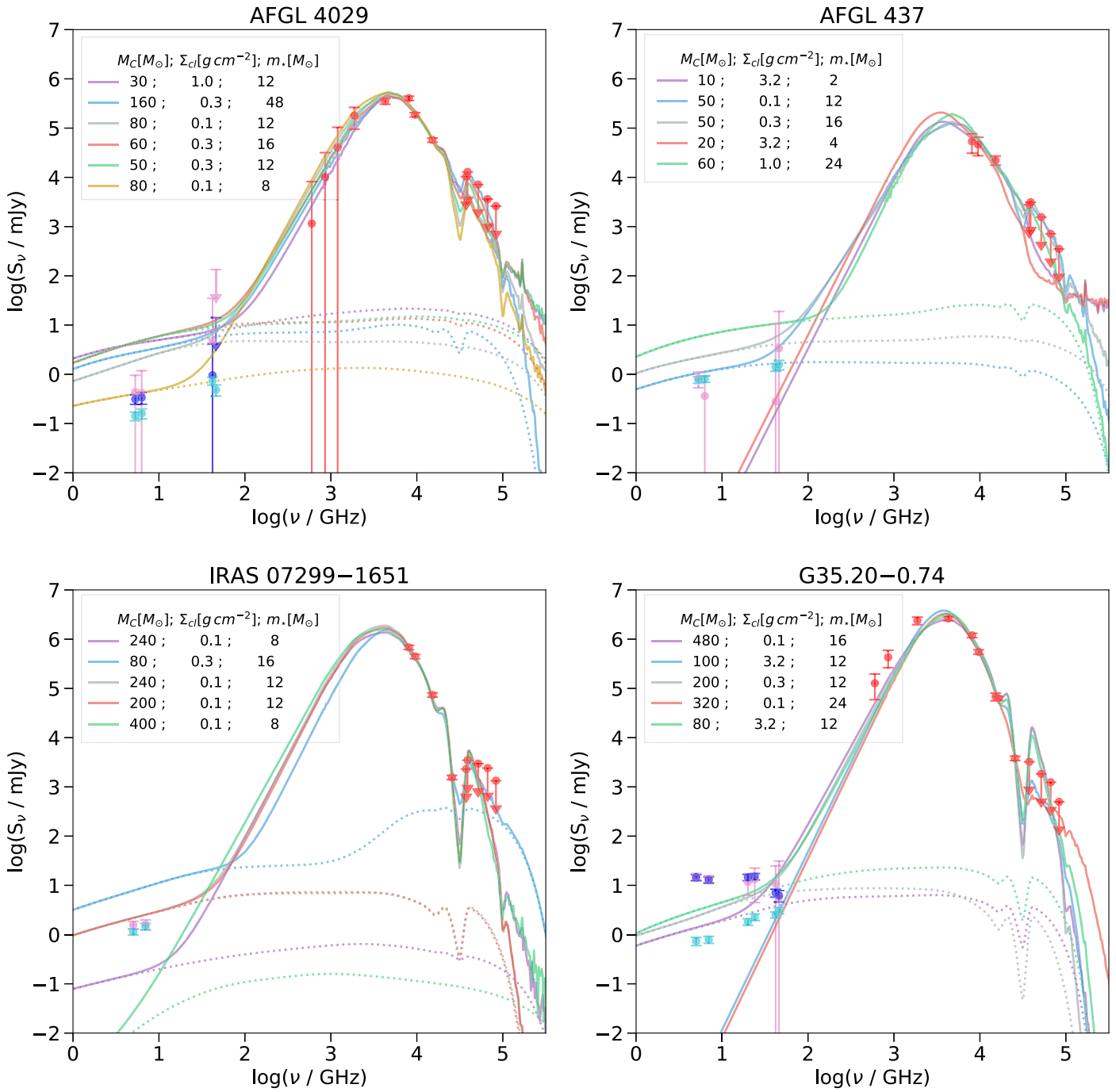

Figure 3. Comprehensive SEDs and models of the protostars. Red circles show IR data for the SOMA apertures as measured by DLT17. Solid colored lines are best fits to the IR data (except for yellow lines) from the ZT18 models, which have been augmented by including free–free emission from the TTZ16 model. The dotted colored lines correspond to the estimated free–free component using TTZ16, which only exceeds the thermal dust component at long wavelengths. For sources AFGL 4029 and IRAS 20126+4104, the yellow solid and dotted lines correspond to the best new model estimate of the total emission and the free–free emission, respectively. The colored circles correspond to the flux density as a function of frequency for each scale (magenta: SOMA; blue: *Intermediate*; cyan: *Inner*). Error bars are explained in Section 4.2.

protostellar radiative transfer models. As explained in DLT17, the data at $\lesssim$8 μm are considered to be upper limits because PAH emission and transiently heated small grain emission are not treated well in the ZT models.

In the cases of AFGL 4029 and IRAS 20126+4104, all of the five best models have a predicted radio flux higher than what is observed. In these cases, we analytically select alternative models that are expected to have lower radio fluxes from within the top 20 models from the IR fitting. In general, the free–free flux quickly increases when the photoionized region breaks out the inner disk wind. Therefore, we selected alternative models that are expected to be just before the break-out phase, which is typically at the protostellar mass of $m_* \simeq 10\ (\dot{m}_*/10^{-4}\ M_\odot \mathrm{yr}^{-1})^{0.28}\ M_\odot$ (TTZ16; Tanaka et al. 2017). Ultimately, as in the ZT model for IR and sub-mm wavelengths, we aim to prepare a full suite of model grids for

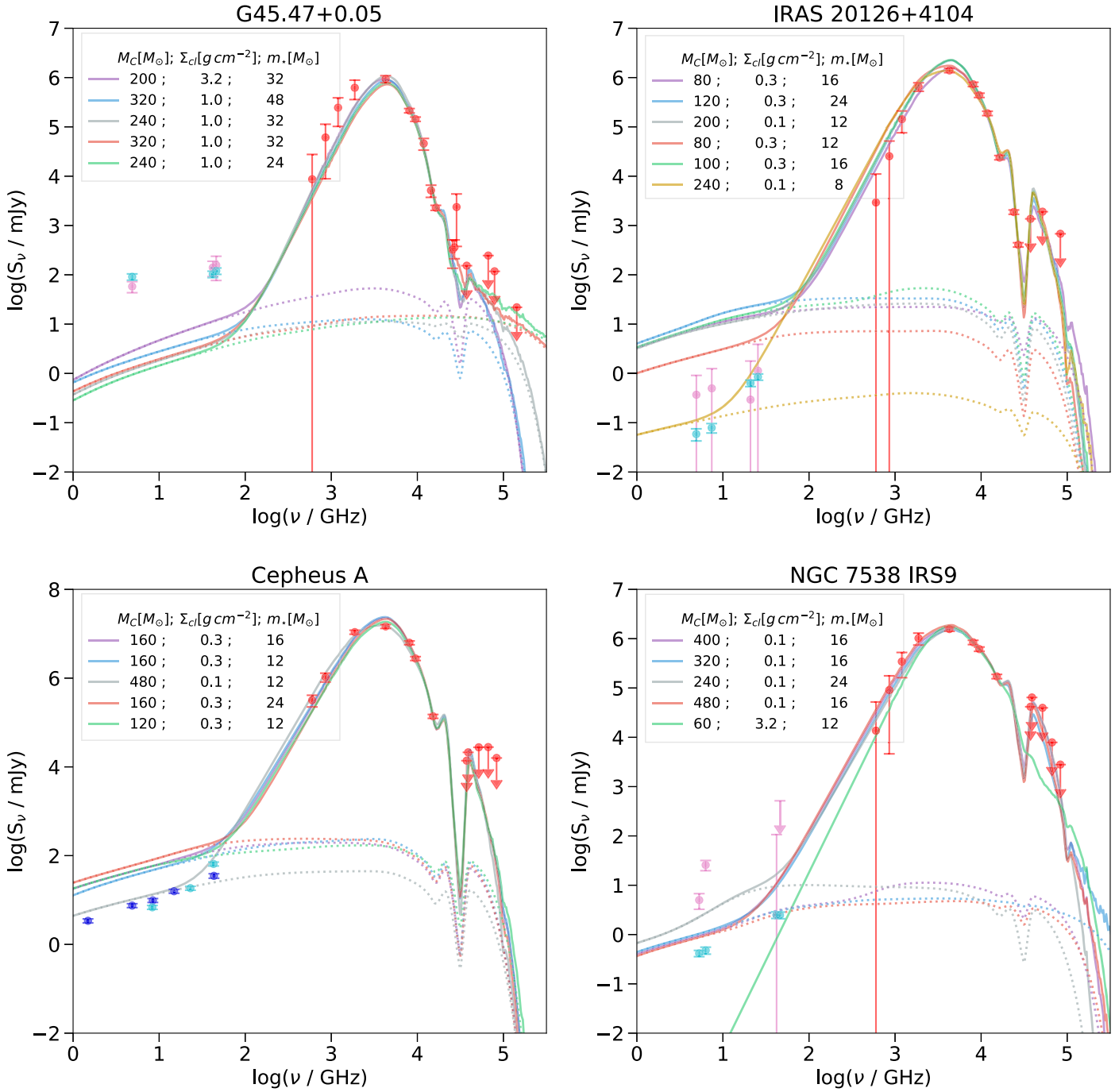

Figure 3. (Continued.)

centimeter wavelengths; however, because this is computationally expensive, we defer it to a future paper.

The parameters of the best-fit ZT models are listed in Table 13, but now ordered from best to worst as measured by the reduced χ^2 from the *Inner* scale ($\chi^2_{\rm all\_inner}$). This is because the ZT and TTZ16 models are developed assuming a single protostar within a core and with a focus on the inner regions. The reduced χ^2 is estimated using Equation (4) from Zhang & Tan (2018). The radio data occurring within the same band (i.e., with very similar frequencies) were averaged together to give more equal weight over the SED.

5.1. Comparing Models with Data

We now describe the results of the TTZ16 models for each of the eight regions using the best five models from the ZT grid as examples, except for AFGL 4029 and IRAS 20126+4104 where we had to identify a best overall model from the ZT results that is beyond the best five (but within the best 20 results). We center our attention on the results from the *Inner* scale because the TTZ16 model assumes that a prestellar core collapses to form a single high-mass star, and it is mostly focused on the inner regions.

AFGL 4029: The two best-fit models using MIR to FIR data alone to build the SED have $\chi^2_{\rm IR} = 1.07$ and 1.16, and have

Table 13
Parameters of the Best-fitted Models of Zhang & Tan and Tanaka et al. (2016)

Region	$\chi^2_{\rm all\_inner}$	$\chi^2_{\rm all\_inter}$	$\chi^2_{\rm all\_SOMA}$	$\chi^2_{\rm IR}$	M_c ($M_\odot$)	$\Sigma_{\rm cl}$ (g cm^{-2})	R_c (pc)($''$)	$m_\star$ ($M_\odot$)	$\theta_{\rm view}$ (°)	A_V (mag)	$M_{\rm env}$ ($M_\odot$)	$\theta_{\rm w,esc}$ (°)	$\dot{M}_{\rm disk}$ (10^{-4} $M_\odot$ yr^{-1})	L_{bol} (10^4 $L_\odot$)
AFGL 4029	11.07	1.71	1.62	1.74	80	0.1	0.21(22)	8	74	0.0	62	27	0.5	0.97
	36.87	9.03	1.51	1.36	80	0.1	0.21(21)	12	88	0.0	47	40	0.5	1.6
	43.55	12.31	1.52	1.16	160	0.3	0.17(17)	48	88	15.2	14	77	1.1	0.34
	51.95	16.83	1.68	1.07	30	1.0	0.04(4)	12	62	13.1	6	53	1.9	4.1
	58.35	18.29	2.16	1.55	50	0.3	0.09(10)	12	51	15.2	22	46	1.0	2.4
	60.05	18.02	2.08	1.47	60	0.3	0.10(10)	16	62	4.0	19	56	1.1	3.6
AFGL 437	4.52	···	0.42	0.29	50	0.1	0.16(17)	12	80	7.5	15	59	0.3	1.4
	17.89	···	1.66	0.32	50	0.3	0.09(9)	16	77	2.6	8	68	0.7	3.1
	49.37	···	5.28	0.53	60	1.0	0.06(6)	24	89	16.8	5	71	1.9	9.3
	334.54	···	36.74	0.51	20	3.2	0.02(2)	4	39	0.0	12	34	3.1	0.3
	399.67	···	42.59	0.04	10	3.2	0.01(1)	2	39	0.0	6	35	1.8	0.3
IRAS 07299	3.46	···	1.47	0.90	240	0.1	0.36(44)	12	89	48.5	211	19	0.9	2.0
	3.54	···	1.59	1.07	200	0.1	0.33(40)	12	89	51.5	174	20	0.8	2.0
	22.65	···	16.42	0.62	240	0.1	0.36(44)	8	89	6.1	226	13	0.7	1.1
	26.21	···	13.07	0.86	80	0.3	0.12(14)	16	89	12.1	42	42	1.5	4.2
	70.69	···	46.46	1.16	400	0.1	0.47(57)	8	62	0.0	386	10	0.8	1.0
G35.20−0.74	19.35	34.03	21.00	2.60	480	0.1	0.51(48)	16	48	40.4	440	15	1.2	3.9
	26.10	19.89	13.05	2.76	200	0.3	0.19(17)	12	22	43.4	173	17	1.9	4.0
	33.14	15.25	9.85	2.79	80	3.2	0.04(3)	12	39	15.2	58	22	8.4	5.0
	135.79	472.57	328.48	2.62	100	3.2	0.04(4)	12	34	28.3	77	20	9.4	5.2
	158.33	521.58	356.98	2.78	320	0.1	0.42(39)	24	68	81.8	256	27	1.2	8.4
G45.47+0.05	40.94	···	9.53	1.20	200	3.2	0.06(1)	32	89	61.6	140	25	16.9	46.0
	57.05	···	12.91	1.33	320	1.0	0.13(3)	48	89	46.5	200	35	9.3	50.9
	68.80	···	15.74	1.68	320	1.0	0.13(3)	32	68	15.2	252	24	8.2	27.4
	71.24	···	16.22	1.62	240	1.0	0.11(3)	32	83	2.0	170	30	7.2	25.7
	79.60	···	18.14	1.71	240	1.0	0.11(3)	24	55	0.0	192	23	6.6	17.2
IRAS 20126	5.42	···	2.99	3.38	240	0.1	0.36(45)	8	71	24.2	226	13	0.7	1.0
	53.82	···	2.48	2.38	80	0.3	0.12(15)	12	44	73.7	53	31	1.4	3.4
	106.35	···	3.44	2.29	200	0.1	0.33(41)	12	89	65.7	174	20	0.8	2.0
	110.91	···	3.21	1.88	80	0.3	0.12(15)	16	80	33.3	42	42	1.5	4.2
	117.92	···	3.70	2.40	100	0.3	0.13(16)	16	51	68.7	61	36	1.6	4.5
	136.40	···	3.86	2.16	120	0.3	0.14(18)	24	74	69.7	57	47	1.8	9.3
Cepheus A	7.13	9.18	···	2.43	480	0.1	0.51(150)	12	89	84.8	457	12	1.1	2.4
	50.64	72.00	···	2.31	160	0.3	0.17(49)	12	29	100.0	135	20	1.8	3.8
	57.36	89.49	···	3.06	120	0.3	0.14(42)	12	65	62.6	93	24	1.6	3.6
	63.71	93.12	···	2.23	160	0.3	0.17(49)	16	44	95.9	125	26	2.0	5.0
	85.10	126.97	···	2.78	160	0.3	0.17(49)	24	83	100.0	98	37	2.2	9.9
NGC 7538	13.18	···	2.83	0.19	320	0.1	0.42(32)	16	39	2.02	281	19	1.1	3.7
	14.32	···	3.09	0.15	400	0.1	0.47(36)	16	22	22.2	364	17	1.1	3.8
	14.44	···	3.52	0.42	480	0.1	0.51(40)	16	22	18.2	440	15	1.2	3.8
	31.35	···	1.22	0.35	240	0.1	0.36(28)	24	39	52.5	171	33	1.1	8.2
	149.39	···	66.64	0.53	60	3.2	0.03(2)	12	34	21.2	38	27	7.6	5.0

Note. Models are listed from best to worst, as measured by the reduced χ^2 from the *Inner* scale ($\chi^2_{\rm all\_inner}$) of each region. Parameters $\chi^2_{\rm IR}$, $\theta_{\rm view}$, and A_V from the five best models reported in DLT17 have been updated to reflect upgrades in the ZT model. First models for sources AFGL 4029 and IRAS 20126+4104 are new estimates corresponding to better fits (see Section 5).

parameters of protostellar mass $m_\star$= 12 and 48 $M_\odot$, core mass M_c = 30 and 160 $M_\odot$, and $\Sigma_{\rm cl}$ = 0.3 and 1 g cm^{-2} clumps, respectively. Including the centimeter continuum fluxes to better cover the SED, we can see in Figure 3 that the five best models seem to be overestimating the expected free–free emission by ∼1 dex. Therefore, after exploring other resulting models from the DLT17 study, we found a matching model with $\chi^2_{\rm IR}$ = 1.74 and $\chi^2_{\rm all\_inner}$ = 11.07, which yields protostellar parameters of $m_\star$ = 8 $M_\odot$, a relatively low mass of the core (M_c = 80 $M_\odot$) and $\Sigma_{\rm cl}$ = 0.1 g cm^2, accreting at 5 × 10^{-5} $M_\odot$ yr^{-1} and a bolometric luminosity of ∼10^4 $L_\odot$.

AFGL 437S: For source AFGL 437S, we lack reliable FIR measurements at wavelengths >40 μm (see above) and we have only three effective data points (plus the 3–8 μm data treated as upper limits), so the results from the ZT models in this case are not constrained very well. In this specific case, we benefit greatly from the centimeter emission to refine our results. The best-fit model using MIR data alone has $\chi^2_{\rm IR}$ = 0.04 and produces parameters of $m_\star$ = 2 $M_\odot$, a core of mass M_c = 10 $M_\odot$, and $\Sigma_{\rm cl}$ = 3.2 g cm^{-2} clump. However, we disfavor this model because it is obvious from the radio observations that this source has a temperature high enough to emit UV photons and has already formed an UC/HC H II region. Therefore, our best-matching model, as based on the $\chi^2_{\rm IR}$ = 0.29 and $\chi^2_{\rm all\_inner}$ = 4.52, has $m_\star$ = 12 $M_\odot$, a core of mass M_c = 50 $M_\odot$, and $\Sigma_{\rm cl}$ = 0.1 g cm^{-2} clump. These

parameters are also more consistent with those reported by Kumar Dewangan & Anandarao (2010).

IRAS 07299-1651: This source also has a relatively limited amount of data in the FIR and in the centimeter to constrain the models. The five best ZT models using only the IR data indicate that a protostar in the range of 8–16 $M_\odot$, in relatively low-Σ clumps, and mainly in cores of more than a couple hundred solar masses can fit the observations well. When including our centimeter-wavelength emission for this source, our best-matching model has $\chi^2_{\rm IR} = 0.90$ and $\chi^2_{\rm all\_inner} = 3.46$ with parameters of $m_\star = 12\,M_\odot$, a core of mass $M_c = 240\,M_\odot$, and a $\Sigma_{\rm cl} = 0.1\,{\rm g\,cm^{-2}}$ clump. A similar fit is given by the second-best model, based on the $\chi^2_{\rm all\_inner} = 3.54$, with the only difference being the mass of the core is slightly lower.

G35.20–0.74: The best-fit model using the IR SED alone also corresponds to the best-matching model when adding the centimeter data emission with $\chi^2_{\rm IR} = 2.60$ and $\chi^2_{\rm all\_inner} = 19.35$ with parameters of $m_\star = 16\,M_\odot$, a core of mass $M_c = 480\,M_\odot$, and a $\Sigma_{\rm cl} = 0.1\,{\rm g\,cm^{-2}}$ clump. The source detected at the *Inner* scale (or source 8a in Beltrán et al. 2016) is slightly extended at 6 cm, and it is blended with other components; however, it is a point source at 1.3 cm and 0.7 cm. Thus, it is possible that we are missing part of the flux at 6 cm, and this may explain why the models seem to overestimate the expected free–free emission at 6 cm. Our resulting protostellar mass of 16 $M_\odot$ is consistent with the value of of 18 $M_\odot$ estimated by Sánchez-Monge et al. (2013) when fitting the velocity field of the core with a rotating Keplerian disk, although they argue that this value corresponds to the total mass of a binary system in core B. Our results disfavor the models with protostellar mass $m_\star = 12\,M_\odot$ and with relatively low core masses and high $\Sigma_{\rm cl}$ clumps, because the expected free–free emission for these models is many orders of magnitude lower than the observed one.

G45.47+00.05: The observed centimeter continuum emission from G45.47+00.05S (which is the dominant source in the region) is significantly higher (by a few orders of magnitude) than the predicted free–free emission from any of our IR-derived ZT models. This is despite the fact that the best two models from the ZT results already predict a rather high-mass protostar in the range of 30–50 $M_\odot$ embedded in a massive core, a relatively high Σ clump, and low accretion rates in the range of $\sim 10^{-5}\,M_\odot\,{\rm yr^{-1}}$. Among the eight sources presented in this study, this is the only case where none of the free–free models can describe the centimeter emission observed in the source. This region is also the most luminous and likely the most evolved one in this sample, which leads us to think that the radio emission from this source may be boosted by the process of photoevaporation. Photoevaporation is not yet accounted for in the TTZ model, which only considered photoionization of the magnetocentrifugally driven wind. However, as the protostar increases its mass above $\sim 20\,M_\odot$, the ionizing radiation becomes dramatically stronger, creating a photoevaporation flow from the disk and infall envelope that is exposed by the outflow cavity wall, i.e., a wind driven by ionized gas-pressure. By enhancing the mass of ionized gas, the centimeter continuum emission is expected to be much higher than that predicted by the TTZ model without such a photoevaporation flow.

IRAS 20126+4104: Including the centimeter continuum fluxes to better sample the SED, we can see in Figure 3 that the best five models seem to be overestimating the expected free–free emission. Therefore, after exploring other resulting models from the DLT17 study and the ZT models, we found a matching model with $\chi^2_{\rm IR} = 3.38$ and $\chi^2_{\rm all\_inner} = 5.42$, which yields protostellar parameters of $m_\star = 8\,M_\odot$, core mass $M_c = 240\,M_\odot$, and $\Sigma_{\rm cl} = 0.1\,{\rm g\,cm^{-2}}$. This protostellar mass is consistent with the value of 7–10 $M_\odot$ estimated by Cesaroni et al. (2005), Moscadelli et al. (2011), and Cesaroni et al. (2014) from methyl cyanide emission that is likely tracing a Keplerian disk around the protostar. However, with similar methods, Chen et al. (2016) estimated a protostellar mass of 12 $M_\odot$. Therefore, either of our two best models presented in Table 13 for this source could be applicable.

Cepheus A: The best-matching model for this source after using the extended SED from centimeter to NIR emission has $\chi^2_{\rm IR} = 2.43$ and $\chi^2_{\rm all\_inner} = 7.13$ and is constrained to a protostellar mass of $m_\star = 12\,M_\odot$, a relatively massive core of $M_c = 480\,M_\odot$, and a $\Sigma_{\rm cl} = 0.1\,{\rm g\,cm^{-2}}$ clump. Our result is consistent with the kinematic masses estimated for the central source HW2, which are in the range of 10–20 $M_\odot$ (e.g., Sanna et al. 2017).

NGC 7538 IRS9: Our results using the extended SED favor all our models with a protostellar mass of $m_\star = 16\,M_\odot$, with a relatively massive core in the range of 320–480 $M_\odot$, and a $\Sigma_{\rm cl} = 0.1\,{\rm g\,cm^{-2}}$ clump. Based on our results, we disfavor the model that has a 12 $M_\odot$ protostar, embedded in a core of $M_c = 60\,M_\odot$, with a $\Sigma_{\rm cl} = 3.2\,{\rm g\,cm^{-2}}$ clump, because the predicted free–free emission from such model is significantly lower than the observed one.

6. Discussion

DLT17 tested the ZT radiative transfer model by fitting MIR and FIR data on the same sample that we present in this paper. By obtaining good fits to the data, they showed that high-mass protostar models based on core accretion that are physically self-consistent and scaled-up from those developed for lower-mass protostars can act as a reasonable description of the sources. However, these solutions from simple SEDs are not unique and yield a range of values for the main parameters that need to be further constrained. Centimeter continuum emission is expected even for early stages in the formation of high-mass stars (see Rosero et al. 2016) and we have utilized it here as an important extra diagnostic and test of the protostellar models, i.e., of their ionizing luminosity. Using the initial range of parameters that resulted from the ZT model, we were able to use the TTZ16 photoionization model to predict the free–free emission expected for these initial conditions. We found that extended SEDs that include longer wavelengths in the centimeter regime help to break the degeneracies of the main physical parameters, such as the mass of the core, the mass surface density of the clump, and especially the mass of the protostar. Furthermore, our results are consistent with values estimated from others methods like dynamical protostellar masses.

For the subsample of Type II SOMA sources presented in this paper and that are associated with outflowing material, we generally found protostars in the range of ~8–24 $M_\odot$, except for G45.47+0.05. The centimeter wavelength emission detected toward G45.47+0.05 is brighter than for the rest of the sample and none of the predicted free–free emission models fit these long wavelength observations. We speculate that the origin of the detected radio emission is due to an extra contribution from photoevaporation of the disk and infall

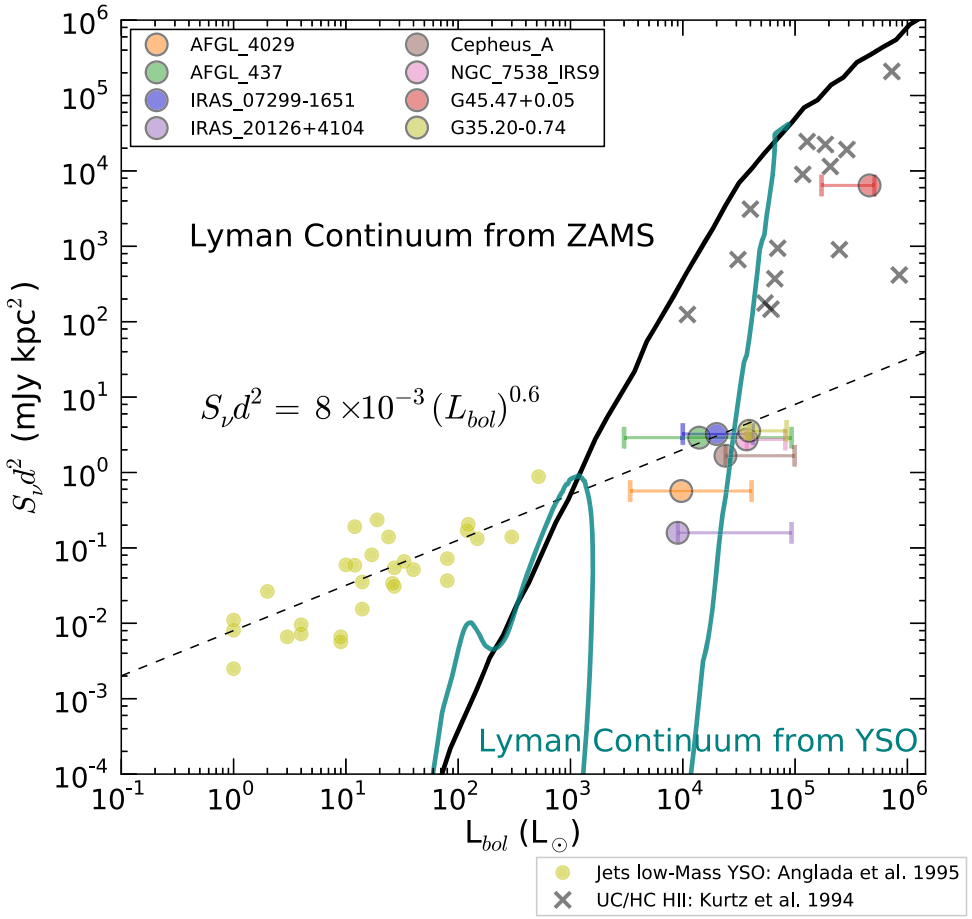

Figure 4. Radio luminosity at 5 GHz for the *Inner* scale as a function of the bolometric luminosity of our eight SOMA sources. The bolometric luminosity is given by our results from the best model (lower χ^2 for the *Inner* scale), and the error bar corresponds to the range of bolometric luminosities of the best models for each source listed in Table 13. The yellow circles represent ionized jets toward low-mass stars from Anglada (1995). The dashed line shows a power-law relation for these sources, given by Anglada et al. (2015): $S_\nu d^2 = 8 \times 10^3 (L_{\rm bol})^{0.6}$. The $\times$ symbols are UC and HC H II regions from Kurtz et al. (1994). The black and the cyan continuous lines are the radio emission expected from optically thin H II regions powered by a ZAMS star (Thompson 1984) and from a YSO (TTZ16), respectively. Note that these models assume all of the ionizing photons are reprocessed by the H II region, i.e., with zero escape fraction.

envelope. However further analysis and modeling is required to fully understand its nature. For instance, an observational diagnostic to differentiate between a MHD disk wind and a photoevaporation flow is through the width of hydrogen recombination lines. A disk wind driven by magnetocentrifugal forces provides a broader width of $>100\,{\rm km\,s^{-1}}$ (Jiménez-Serra et al. 2011), while a photoevaporation flow has a narrower profile of $<100\,{\rm km\,s^{-1}}$ (Guzmán et al. 2014). From the modeling side, we defer the analysis of more evolved sources that require the addition of photoevaporation components in the TTZ16 to a later study. We also note that contributions from shock ionization, which may be especially pertinent for the relatively weak centimeter emission in extended jet knots, are not yet included in the models.

As an additional diagnostic to understand the nature of our sources, in Figure 4 we compare the bolometric luminosity with the radio luminosity at 5 GHz from the *Inner* scale of our eight SOMA sources (the fluxes have been scaled to $\nu = 5$ GHz using the spectral index estimated at that scale). The bolometric luminosity is given by our results for the best model (lowest χ^2 for the *Inner* scale) and the error bar corresponds to the range of bolometric luminosities from the models listed in Table 13. Additionally, we use yellow circles to indicate the radio luminosity from lower-mass protostars associated with ionized jets from Anglada (1995). We scaled their fluxes from 3.6 cm, using a factor of 0.74, assuming that those sources have a spectral index $\alpha = 0.6$, which is the canonical value of ionized jets. A power-law fit to these data of $S_\nu d^2 = 8 \times 10^3 (L_{\rm bol})^{0.6}$ is shown with a dashed line. We also show several UC/HC H II regions from Kurtz et al. (1994), represented with $\times$ symbol. The continuous black line is the radio emission from an optically thin H II region, given the expected Lyman continuum luminosity of a single ZAMS star at a given luminosity (Thompson 1984). The cyan continuous line corresponds to the expected radio emission that arises from photoionization from a protostar, as predicted by the TTZ16 model, also for optically thin conditions at 5 GHz. This specific evolutionary stellar model corresponds to the fiducial case, which starts with a core mass of $M_c = 60\,M_\odot$ and a mass surface density with an ambient clump of $\Sigma_{\rm cl} = 1\,{\rm g\,cm^{-2}}$.

From Figure 4, we see that the ionized materials toward several of our sources (except G45.47+0.05) appear to follow the same power-law relation found by Anglada et al. (2015), which may indicate that a universal mechanism based on shock ionization (see Anglada et al. 2018 for a review) is still relevant for these sources. However, they also match quite well with the example model (cyan line) from TTZ16, which is based on photoionization. One must bear in mind that there is a very

large dynamic range present for the radio luminosities. A more comprehensive theoretical model that includes both shock and photoionization may be needed to better model these sources. Still, at the highest bolometric luminosities, i.e., as sampled by G45.47+0.05, it seems likely that the sources are in a photoionization-dominated regime, and a photoionized outflow model may be relevant to many HC H II region sources. We note that, in our detailed modeling of radio SEDs as applied to the sources, there is typically a high escape fraction of ionizing photons from the source, as well as loss of ionizing photons due to absorption by dust. Thus, these models are generally lower in their radio flux than the simple extrapolation shown in Figure 4 by the cyan line. As we have mentioned earlier, our detailed models likely need an additional photoevaporative flow component to be able to explain the strong radio fluxes of the source of G45.47+0.05.

Our main interest for this paper has been to measure the flux density of the centimeter continuum sources associated with our regions and compare them to the predicted free–free emission from the TTZ16 model using the initial parameters from the best-fitting results of the ZT model presented in DLT17. Additionally, for completeness, we have measured the flux densities of the detected radio sources at three defined scales: the SOMA scale, which has the same size radius used for the IR photometry for each region; the *Intermediate* scale, which measures the flux density of radio detections that appear aligned and that may be part of a radio jet; and the *Inner* scale, which is the most localized region around the central protostar. This approach helps us understand whether the central source is the more dominant one in the SOMA scale, or if there are perhaps other protostellar sources adding to the centimeter continuum emission—as we think is the case of G35.20−0.74, and possibly NGC 7538 IRS9 and IRAS 20126+4104.

We have also attempted to understand the nature of the detected radio continuum sources, but due to the differences in resolution of our data at the given frequencies (except for regions G35.20−0.74 and IRAS 20126+4104), we are not able to make reliable estimates of the spectral indices at the different scales studied in this paper. However, if most of the detected radio sources associated with our *Inner* scale have a jet nature, we will expect them to be more compact at *Q*-band because ionized jets have a gradient of density and are partially optically thick. Thus, we expect the base of the jet to be smaller at higher frequencies. In order to determine reliable spectral indices, we require data with similar resolutions that can be sensitive to the same scales.

We can also use these data to investigate multiplicity. For all regions except AFGL 437, at least two sources are detected within the SOMA scale at the lower frequencies (i.e., 6 cm data). Several of these detections appear elongated in the same direction as the associated molecular outflow, e.g., in the case of AFGL 4029, G35.20−0.74, IRAS 20126+4104, and Cepheus A. Thus, it is very likely that the central radio source at the *Inner* scale corresponds to the base of the ionized jet, and the aligned radio sources (if any) correspond to knots of the jet. This could also be the case for IRAS 07299−1651, although at the moment we can not rule out the possibility that the extended emission in our image for this region is due to calibration errors. Thus, for the above sources, there is no strong evidence for stellar multiplicity. On somewhat larger scales, in some sources, we find evidence for other stellar sources. Together with information from the literature, our presented data reveal the detection of several variable radio sources within the SOMA scale, e.g., in AFGL 4029 and NGC 7538 IRS9. Furthermore, IRAS 20126+4104 has at least two of these variable radio sources that have spectral indices that are consistent with non-thermal emission and are surrounding the high-mass protostar located at the center of the core. One possible scenario for these radio variable sources, at least for those located at distances <2 kpc, is that they correspond to flaring T-Tauri stars, indicating the presence of a few lower-mass YSOs in the vicinity, at least in projection, of the high-mass protostar. The detectability (i.e., at 5σ signal to noise ratio) of low-mass protostars in this sample is analyzed using the results of the Gould Belt survey, which is a large sample of low-mass YSOs observed with the VLA at 4.5 and 7.5 GHz (Dzib et al. 2013, 2015; Kounkel et al. 2014; Ortiz-León et al. 2015; Pech et al. 2016). Of the bright low-mass protostars detected in the Gould Belt survey, the two brightest ones are class III YSOs located in the Ophiuchus region with $S_{7.5\,\mathrm{GHz}} = 8.51$ mJy and 7.1 mJy (Dzib et al. 2013). We find that such objects could be detected in our combined *C*-band images at level of $\sim 5\sigma$, based on an average distance of $\sim$1.8 kpc and average image rms of 6 μJy/beam, but would not be detectable in our images at higher frequencies. This analysis applies to five regions (i.e., AFGL 4029, AFGL 437, IRAS 07299-1651, G35.20-0.74, and IRAS 20126+4104), for which the *C*-band sensitivities and distances are very similar (to about $\pm$20%). We expect to be sensitive to such objects everywhere within the SOMA scale for these five regions because the noise in the primary beam-corrected *C*-band image is essentially constant ($\sim$2%). Furthermore, these images have no bright sources causing sidelobes within the SOMA scale, so we do not think that dynamic range is an issue in the detection of low-mass protostars at the levels presented above. For the other three regions, we either do not have data at *C*-band, or the images have lower sensitivity and therefore a detection of such objects is not expected, although we cannot rule out the presence of T-Tauri stars brighter than those detected in the Gould Belt survey. Deeper VLA observations are needed for all the SOMA regions in order to place more stringent constraints on the low-mass YSO population, but the current observations provide no evidence for rich clusters of such YSOs around the high-mass protostars.

7. Summary

We have presented a pilot study mainly using public archival interferometry data from the VLA to build extended SEDs from centimeter emission to FIR, in order to test theoretical models of high-mass star formation forming via core accretion, particularly the TTZ16 and ZT18 models. The TTZ16 model reproduces the SEDs of the IR and radio data for early-type sources before the existence of a strongly photoevaporated flow contribution, which is not yet part of the model. Our results indicate that centimeter continuum emission is effective at breaking degeneracies encountered in the IR-only analysis of the main physical parameters, such as the mass of the core, the mass surface density of the clump, and the mass of the protostar, with the main diagnostic power coming from the strong dependence of ionizing luminosity of the protostars as a function of the protostellar mass (though the accretion rate also influences this, given its effect on protostellar evolution). Moreover, these resulting estimates of protostellar masses

appear more consistent with values obtained from other independent methods, such as dynamical mass estimates.

We also probed the presence of stellar multiplicity, which is expected to vary between core accretion and competitive accretion models of high-mass star formation. We do not see large numbers of radio sources that are likely to be other protostars or young stars around the primary target, although a few lower-mass sources—perhaps variable T-Tauri stars—are seen on larger scales around some of the high-mass protostars. Of course, for these distant regions, most low-mass protostars may be too faint to see in the cm continuum, so deeper observations are needed to better explore stellar multiplicity around these high-mass protostars.

Also, in order to make a more uniform and systematic study of the sources, and specifically to understand the nature of the centimeter wavelength emission associated with the SOMA survey regions and interpret the centimeter continuum using the TTZ16 models, it will be ideal to have similar resolutions and to be sensitive to similar scales. Expanding the sample size beyond the eight sources presented here is also a high priority.

J.C.T. acknowledges support from NSF grant AST 1411527 and several USRA/SOFIA grants in support of the SOMA survey. K.E.I.T. acknowledges support from NAOJ ALMA Scientific Research grant No. 2017−05A. This research made use of APLpy, an open-source plotting package for Python hosted at http://aplpy.github.com. We also thank the anonymous referee, whose comments improved this manuscript.

Software: CASA (McMullin et al. 2007), APLpy (Robitaille & Bressert 2012), HOCHUNK3d (Whitney et al. 2003, 2013), CLOUDY (Ferland et al. 2013).

ORCID iDs

V. Rosero https://orcid.org/0000-0001-8596-1756
K. E. I. Tanaka https://orcid.org/0000-0002-6907-0926
J. C. Tan https://orcid.org/0000-0002-3389-9142
J. Marvil https://orcid.org/0000-0003-1111-8066
M. Liu https://orcid.org/0000-0001-6159-2394
Y. Zhang https://orcid.org/0000-0001-7511-0034
J. M. De Buizer https://orcid.org/0000-0001-7378-4430
M. T. Beltrán https://orcid.org/0000-0003-3315-5626

References

Anglada, G. 1995, RMxAC, 27, 67
Anglada, G., Rodríguez, L. F., & Carrasco-Gonzalez, C. 2015, in Advancing Astrophysics with the Square Kilometre Array (AASKA14), The Cradle of Life (Trieste: SISSA), 121
Anglada, G., Rodríguez, L. F., & Carrasco-González, C. 2018, A&ARv, 26, 3
Anglada, G., Villuendas, E., Estalella, R., et al. 1998, AJ, 116, 2953
Bally, J., & Zinnecker, H. 2005, AJ, 129, 2281
Beltrán, M. T., Cesaroni, R., Moscadelli, L., et al. 2016, A&A, 593, A49
Blandford, R. D., & Payne, D. G. 1982, MNRAS, 199, 883
Bonnell, I. A., Bate, M. R., Clarke, C. J., & Pringle, J. E. 2001, MNRAS, 323, 785
Bonnell, I. A., Bate, M. R., & Zinnecker, H. 1998, MNRAS, 298, 93
Brogan, C. L., Hunter, T. R., Cyganowski, C. J., et al. 2016, ApJ, 832, 187
Castelli, F., & Kurucz, R. L. 2004, arXiv:astro-ph/0405087
Cesaroni, R., Felli, M., Testi, L., Walmsley, C. M., & Olmi, L. 1997, A&A, 325, 725
Cesaroni, R., Galli, D., Neri, R., & Walmsley, C. M. 2014, A&A, 566, A73
Cesaroni, R., Neri, R., Olmi, L., et al. 2005, A&A, 434, 1039
Chen, H.-R. V., Keto, E., Zhang, Q., et al. 2016, ApJ, 823, 125
Cunningham, A. J., Klein, R. I., Krumholz, M. R., & McKee, C. F. 2011, ApJ, 740, 107
Curiel, S., Ho, P. T. P., Patel, N. A., et al. 2006, ApJ, 638, 878
Dale, J. E., Bonnell, I. A., Clarke, C. J., & Bate, M. R. 2005, MNRAS, 358, 291
De Buizer, J. M., Liu, M., Tan, J. C., et al. 2017, ApJ, 843, 33
Dzib, S. A., Loinard, L., Mioduszewski, A. J., et al. 2013, ApJ, 775, 63
Dzib, S. A., Loinard, L., Rodríguez, L. F., et al. 2015, ApJ, 801, 91
Ferland, G. J., Porter, R. L., van Hoof, P. A. M., et al. 2013, RMxAA, 49, 137
Gibb, A. G., Hoare, M. G., Little, L. T., & Wright, M. C. H. 2003, MNRAS, 339, 1011
Ginsburg, A., Bally, J., & Williams, J. P. 2011, MNRAS, 418, 2121
Gómez, J. F., Sargent, A. I., Torrelles, J. M., et al. 1999, ApJ, 514, 287
Gomez, J. F., Torrelles, J. M., Estalella, R., et al. 1992, ApJ, 397, 492
Guzmán, A. E., Garay, G., Rodríguez, L. F., et al. 2014, ApJ, 796, 117
Hoare, M. G., Lumsden, S. L., Oudmaijer, R. D., et al. 2005, in IAU Symp. 227, Massive Star Birth: A Crossroads of Astrophysics, ed. R. Cesaroni et al. (Cambridge: Cambridge Univ. Press), 370
Hofner, P., Cesaroni, R., Olmi, L., et al. 2007, A&A, 465, 197
Hosokawa, T., & Omukai, K. 2009, ApJ, 703, 1810
Hosokawa, T., Yorke, H. W., & Omukai, K. 2010, ApJ, 721, 478
Jiménez-Serra, I., Martín-Pintado, J., Báez-Rubio, A., Patel, N., & Thum, C. 2011, ApJL, 732, L27
Keto, E. 2007, ApJ, 666, 976
Kölligan, A., & Kuiper, R. 2018, A&A, 620, A182
Kounkel, M., Hartmann, L., Loinard, L., et al. 2014, ApJ, 790, 49
Kuiper, R., & Hosokawa, T. 2018, A&A, 616, A101
Kuiper, R., Turner, N. J., & Yorke, H. W. 2016, ApJ, 832, 40
Kumar Dewangan, L., & Anandarao, B. G. 2010, MNRAS, 402, 2583
Kurtz, S., Churchwell, E., & Wood, D. O. S. 1994, ApJS, 91, 659
Manjarrez, G., Gómez, J. F., & de Gregorio-Monsalvo, I. 2012, MNRAS, 419, 3338
Matsushita, Y., Machida, M. N., Sakurai, Y., & Hosokawa, T. 2017, MNRAS, 470, 1026
Matzner, C. D., & McKee, C. F. 2000, ApJ, 545, 364
McKee, C. F., & Tan, J. C. 2003, ApJ, 585, 850
McLaughlin, D. E., & Pudritz, R. E. 1997, ApJ, 476, 750
McMullin, J. P., Waters, B., Schiebel, D., Young, W., & Golap, K. 2007, in ASP Conf. Ser. 376, Astronomical Data Analysis Software and Systems XVI, ed. R. A. Shaw, F. Hill, & D. J. Bell (San Francisco, CA: ASP), 127
Moscadelli, L., Cesaroni, R., Rioja, M. J., Dodson, R., & Reid, M. J. 2011, A&A, 526, A66
Mottram, J. C., Hoare, M. G., Lumsden, S. L., et al. 2007, A&A, 476, 1019
Ortiz-León, G. N., Loinard, L., Mioduszewski, A. J., et al. 2015, ApJ, 805, 9
Patel, N. A., Curiel, S., Sridharan, T. K., et al. 2005, Natur, 437, 109
Pech, G., Loinard, L., Dzib, S. A., et al. 2016, ApJ, 818, 116
Perley, R. A., & Butler, B. J. 2013, ApJS, 204, 19
Price, S. D., Egan, M. P., Carey, S. J., Mizuno, D. R., & Kuchar, T. A. 2001, AJ, 121, 2819
Purcell, C. R., Hoare, M. G., & Diamond, P. 2008, in ASP Conf. Ser. 387, Massive Star Formation: Observations Confront Theory, ed. H. Beuther, H. Linz, & T. Henning (San Francisco, CA: ASP), 389
Qin, S.-L., Wang, J.-J., Zhao, G., Miller, M., & Zhao, J.-H. 2008, A&A, 484, 361
Ray, T. P., Poetzel, R., Solf, J., & Mundt, R. 1990, ApJL, 357, L45
Reynolds, S. P. 1986, ApJ, 304, 713
Robitaille, T., & Bressert, E. 2012, APLpy: Astronomical Plotting Library in Python, Astrophysics Source Code Library, ascl:1208.017
Rodriguez, L. F., Garay, G., Curiel, S., et al. 1994, ApJL, 430, L65
Rosero, V., Hofner, P., Claussen, M., et al. 2016, ApJS, 227, 25
Sánchez-Monge, Á, Beltrán, M. T., Cesaroni, R., et al. 2014, A&A, 569, A11
Sánchez-Monge, Á, Cesaroni, R., Beltrán, M. T., et al. 2013, A&A, 552, L10
Sandell, G., Goss, W. M., & Wright, M. 2005, ApJ, 621, 839
Sanna, A., Moscadelli, L., Surcis, G., et al. 2017, A&A, 603, A94
Shakura, N. I., & Sunyaev, R. A. 1973, A&A, 24, 337
Staff, J. E., Tanaka, K. E. I., & Tan, J. C. 2018, arXiv:1811.00954
Stone, J. M., Mihalas, D., & Norman, M. L. 1992, ApJS, 80, 819
Sugiyama, K., Fujisawa, K., Doi, A., et al. 2014, A&A, 562, A82
Tan, J. C., Beltrán, M. T., Caselli, P., et al. 2014, in Protostars and Planets VI, ed. H. Beuther et al. (Tucson, AZ: Univ. Arizona Press), 149
Tan, J. C., & McKee, C. F. 2003, arXiv:astro-ph/0309139
Tanaka, K. E. I., Nakamoto, T., & Omukai, K. 2013, ApJ, 773, 155
Tanaka, K. E. I., Tan, J. C., Staff, J. E., & Zhang, Y. 2017, ApJ, 849, 133
Tanaka, K. E. I., Tan, J. C., & Zhang, Y. 2016, ApJ, 818, 52
Thompson, R. I. 1984, ApJ, 283, 165
Torrelles, J. M., Gomez, J. F., Anglada, G., et al. 1992, ApJ, 392, 616
Towner, A. P. M., Brogan, C. L., Hunter, T. R., et al. 2017, ApJS, 230, 22
Ulrich, R. K. 1976, ApJ, 210, 377
Urquhart, J. S., Hoare, M. G., Purcell, C. R., et al. 2009, A&A, 501, 539

van der Tak, F. F. S., & Menten, K. M. 2005, A&A, 437, 947
Walsh, A. J., Bertoldi, F., Burton, M. G., & Nikola, T. 2001, MNRAS, 326, 36
Walsh, A. J., Burton, M. G., Hyland, A. R., & Robinson, G. 1998, MNRAS, 301, 640
Walsh, A. J., Burton, M. G., Hyland, A. R., & Robinson, G. 1999, MNRAS, 309, 905
Wang, P., Li, Z.-Y., Abel, T., & Nakamura, F. 2010, ApJ, 709, 27
Weintraub, D. A., & Kastner, J. H. 1996, ApJ, 458, 670
Whitney, B. A., Robitaille, T. P., Bjorkman, J. E., et al. 2013, ApJS, 207, 30
Whitney, B. A., Wood, K., Bjorkman, J. E., & Wolff, M. J. 2003, ApJ, 591, 1049
Wilner, D. J., Ho, P. T. P., & Zhang, Q. 1996, ApJ, 462, 339
Wood, D. O. S., & Churchwell, E. 1989, ApJ, 340, 265
Wynn-Williams, C. G., Becklin, E. E., Beichman, C. A., Capps, R., & Shakeshaft, J. R. 1981, ApJ, 246, 801
Zapata, L. A., Fernandez-Lopez, M., Curiel, S., Patel, N., & Rodriguez, L. F. 2013, arXiv:1305.4084
Zapata, L. A., Rodríguez, L. F., & Kurtz, S. E. 2001, RMxAA, 37, 83
Zhang, Y., & Tan, J. C. 2011, ApJ, 733, 55
Zhang, Y., & Tan, J. C. 2018, ApJ, 853, 18
Zhang, Y., Tan, J. C., & Hosokawa, T. 2014, ApJ, 788, 166
Zhang, Y., Tan, J. C., & McKee, C. F. 2013, ApJ, 766, 86